AGU PUBLICATIONS

JGR

Journal of Geophysical Research: Space Physics

RESEARCH ARTICLE

10.1002/2014JA020005

Key Points:
- 3-D global hybrid simulation of near-Earth magnetotail
- Ion injection, dipolarization, and generation of kinetic waves/instabilities
- Systematic dawn-dusk asymmetry exists due to the ion drift effects

Correspondence to:
Y. Lin,
ylin@physics.auburn.edu

Citation:
Lin, Y., X. Y. Wang, S. Lu, J. D. Perez, and Q. Lu (2014), Investigation of storm time magnetotail and ion injection using three-dimensional global hybrid simulation, *J. Geophys. Res. Space Physics*, *119*, 7413–7432, doi:10.1002/2014JA020005.

Received 21 MAR 2014
Accepted 1 SEP 2014
Accepted article online 4 SEP 2014
Published online 22 SEP 2014

Investigation of storm time magnetotail and ion injection using three-dimensional global hybrid simulation

Y. Lin[1], X. Y. Wang[1], S. Lu[2], J. D. Perez[1], and Q. Lu[2]

[1]Physics Department, Auburn University, Auburn, Alabama, USA, [2]Department of Geophysics and Planetary Science, University of Science and Technology of China, Hefei, China

Abstract Dynamics of the near-Earth magnetotail associated with substorms during a period of extended southward interplanetary magnetic field is studied using a three-dimensional (3-D) global hybrid simulation model that includes both the dayside and nightside magnetosphere, for the first time, with physics from the ion kinetic to the global Alfvénic convection scales. It is found that the dayside reconnection leads to the penetration of the dawn-dusk electric field through the magnetopause and thus a thinning of the plasma sheet, followed by the magnetotail reconnection with 3-D, multiple flux ropes. Ion kinetic physics is found to play important roles in the magnetotail dynamics, which leads to the following results: (1) Hall electric fields in the thin current layer cause a systematic dawnward ion drift motion and thus a dawn-dusk asymmetry of the plasma sheet with a higher (lower) density on the dawnside (duskside). Correspondingly, more reconnection occurs on the duskside. Bidirectional fast ions are generated due to acceleration in reconnection, and more high-speed earthward flow injections are found on the duskside than the dawnside. Such finding of the dawn-dusk asymmetry is consistent with recent satellite observations. (2) The injected ions undergo the magnetic gradient and curvature drift in the dipole-like field, forming a ring current. (3) Ion particle distributions reveal multiple populations/beams at various distances in the tail. (4) Dipolarization of the tail magnetic field takes place due to the pileup of the injected magnetic fluxes and thermal pressure of injected ions, where the fast earthward flow is stopped. Oscillation of the dipolarization front is developed at the fast-flow braking, predominantly on the dawnside. (5) Kinetic compressional wave turbulence is present around the dipolarization front. The cross-tail currents break into small-scale structures with $k_\perp \rho_i \sim 1$, where $k_\perp$ is the perpendicular wave number. A sharp dip of magnetic field strength is seen just in front of the sharp rise of the magnetic field at the dipolarization front, mainly on the duskside. (6) A shear flow-type instability is found on the duskside flank of the ring current plasma, whereas a kinetic ballooning instability appears on the dawnside. (7) Shear Alfvén waves and compressional waves are generated from the tail reconnection, and they evolve into kinetic Alfvén waves in the dipole-like field region. Correspondingly, multiple field-aligned current filaments are generated above the auroral ionosphere.

1. Introduction

The Earth's magnetosphere is a complex plasma system with dynamics on a broad range of spatial and temporal scales[*Kivelson and Russell*, 1995]. The physics of the solar wind-magnetosphere interaction is also of multiscale nature, from the particle kinetic scales to the global Alfvénic convection scales. Various boundary layers exist in the vast region of the magnetosphere, including the dayside magnetopause[*Song et al.*, 1995], which plays a major role in the transfer of the solar wind mass, momentum and energy to the Earth, and the magnetotail plasma sheet[*Nishida et al.*, 1998], which connects directly to the ring current[*Daglis et al.*, 1999] and contributes to the radiation belt[*Blake et al.*, 1992; *Baker et al.*, 2006] in the inner magnetosphere.

Geomagnetic substorms are one of the most important global-scale dynamic processes in the magnetosphere. Through the substorm, solar wind energy transmitted from the dayside magnetopause can be released from the magnetotail and injected into the high-latitude ionosphere. Since storms/substorms are conducive to strong particle injections from the tail plasma sheet and variations in the electromagnetic field [*Vassiliadis et al.*, 2002], the magnetotail plasma sheet is also a major particle source of the ring current.

Near-Earth magnetic reconnection and bursty bulk flows (BBFs) [*Angelopoulos et al.*, 1992] are frequently observed in the magnetotail plasma sheet and have been suggested to play important roles in the substorms [*Angelopoulos et al.*, 2008, 2013; *Nishimura et al.*, 2010], although the exact role of the near-Earth

reconnection during substorms is still in debate [*Lui*, 2009]. Accelerated tailward and earthward flows associated with near-Earth reconnection have been observed between 20 and 30 R_E during substorm expansion [*Nagai et al.*, 1998], which indicate the existence of an X line between 20 and 30 R_E in the magnetotail plasma sheet, consistent with the revised near-Earth neutral line model [*Baker et al.*, 1996; *Birn et al.*, 1996]. In the tail-dipole transition region, the taillike field lines are dipolarized as a consequence of the earthward propagation of fast flows and magnetic fluxes. In a multispacecraft observation of dipolarization fronts, *Runov et al.* [2012] find that although the fast flow/front stopped a few R_E beyond geosynchronous orbit, plasma compression propagated farther inward and excited compressional diamagnetic oscillations in the tail-dipole transition region. Dipolarizing flux bundles are observed to propagate earthward at high speed from the reconnection region and are suggested to be the dominant drivers of flux transport [*Liu et al.*, 2014]. Models of plasma bubbles or bubble-blob pairs of entropy variation have been used to understand the earthward penetration of BBFs [*Pontius and Wolf*, 1990; *Wolf et al.*, 2009; *Yang et al.*, 2011; *Birn et al.*, 2011]. Time History of Events and Macroscale Interactions during Substorms (THEMIS) observation of *Panov et al.* [2010] shows multiple overshoot and rebound of a BBF, accompanied by enhancements and depletions of radial pressure gradients. The earthward and tailward flow bursts are found to cause formation of vortices with an opposite sense of rotation.

On the other hand, disruption of the cross-tail current has been identified and also suggested to play a crucial role in initiating the global change associated with the substorm expansion onset [*Lui*, 1996]. Ideal MHD ballooning instability has been proposed to explain the current disruption and explosive growth phase [*Roux*, 1985]. The ballooning modes could be driven by the interaction of the ion pressure gradient with a local region of the "bad" magnetic curvature[*Miura et al.*, 1989] around the transition region between dipolar and taillike field geometry [*Lui*, 1996]. Observations suggest that wave-like auroral enhancements observed before the breakup are likely due to a near-Earth ballooning instability [*Zou et al.*, 2010]. It has also been found that the field line configuration of stretched magnetotail in the substorm growth phase can be unstable to the ballooning onset [*Saito et al.*, 2008]. On the other hand, based on the THEMIS inner tail observations at radial distance $r < 12\ R_E$ for both specific events and statistical results, *Lee et al.* [2012] find that the stretched tail field configurations during the dipolarization growth phase are stable to the interchange mode. Current reduction in the near tail has also been observed by *Tang et al.* [2009] on the basis of a THEMIS substorm event.

MHD models have been used to examine the dynamic evolution of the magnetosphere associated with storms/substorms on the three-dimensional (3-D) global scale [*Walker et al.*, 1993; *Lyon et al.*, 1998; *Pulkkinen et al.*, 1998; *Raeder et al.*, 2001; *Ohtani and Raeder*, 2004; *Hu et al.*, 2007; *Zhu et al.*, 2009; *Ge et al.*, 2011, 2012; *El-Alaoui et al.*, 2013]. The 3-D MHD simulation of *Walker et al.* [1993] is able to show the onset of the tail reconnection and formation of a plasmoid following the dayside reconnection under a southward interplanetary magnetic field (IMF). The simulation of *Lyon et al.* [1998] for an isolated substorm that is driven with the solar wind data finds that the primary energy released is through tail reconnection before the onset. *Pulkkinen et al.* [1998] show that a reconnection region in the midtail is associated with the most intense electrojet currents. The simulation of *Raeder et al.* [2001] for a Geomagnetic Environment Modeling (GEM) substorm challenge event finds a general agreement with the near-Earth neutral line model but suggests that the results critically depend on the Hall and Pederson conductances and anomalous resistivity used in the magnetosphere. *Ohtani and Raeder* [2004] have later revisited this GEM challenge event and found that the near-Earth reconnection causes tail current surge and reduction. Using the global MHD model OpenGGCM, *Ge et al.* [2011] have simulated the substorm process driven by the real-time solar wind and IMF conditions. They show that auroral breakup is caused by the strong flow shear and the flow vortices formed by the BBF flows, with rebound oscillations of the intruding BBFs. The MHD simulation of *El-Alaoui et al.* [2013] shows that strong narrow flow channels are a clear and persistent feature of magnetotail convection which exist at the driving scales for the turbulent spectra. On the other hand, the global MHD simulation of *Zhu et al.* [2009] also suggests that the ballooning instability may play an important role prior to the initial expansion onset of a substorm.

MHD studies, however, are limited to spatial and temporal scales that are much larger than the particle kinetic scales. Nonlinear particle kinetic physics in the global coupling is ignored in the MHD simulations. Ion kinetic physics is important in a number of near-Earth processes associated with the particle injection. When considering magnetic drifts of particles, the frozen-in plasma tube approximation would be invalid

in the near-Earth boundary layers such as the thin plasma sheet current layer. The observed preference of bubble transport to the duskside seems to imply the importance of particle drifts [*Wing and Johnson*, 2009].

McPherron et al. [2011] have scanned the ion flow data during the first pass of the THEMIS D spacecraft to examine the BBFs due to the tail reconnection. Significant dawn-dusk asymmetry is found in the fast flows. Earthward flows are strongly localized in the local time sector 2100–0100 and have a probability distribution identical to that seen in auroral substorm expansions by the IMAGE spacecraft [*Frey et al.*, 2004]. Theories [*Cheng and Lui*, 1998] have shown that in the kinetic description, ballooning instabilities have a threshold β value that is much larger than that predicted by MHD models. The perturbed ion distribution can excite a higher-frequency cross-field current instability. Based on manifestations of high-pressure regions in dipolarized flux tubes, observation of *Sakaguchi et al.* [2011] has led to a speculation that the black aurora patches are linked to the pressure-driven interchange instability, which occurred on the dawnside.

Low-frequency waves can strongly interact with ion particles [*Bauer et al.*, 1995; *Lin and Swift*, 1996; *Angelopoulos et al.*, 2002; *Wygant et al.*, 2002; *Eriksson et al.*, 2004; *Dombeck et al.*, 2005]. Observations of *Takada et al.* [2006] using Cluster spacecraft show that electromagnetic low-frequency waves in the tail lobe close to the plasma sheet boundary layer have Alfvénic properties, and the waves transport their wave energy toward the Earth along magnetic field lines. Kinetic Alfvén waves (KAWs) have been found in plasma sheet boundary layer from observations[*Wygant et al.*, 2002; *Chaston et al.*, 2009], and the generation of KAW-like structures in magnetic reconnection has also been discussed by simulations [*Shay et al.*, 2011]. *Chaston et al.* [2012] have reported observations from the THEMIS spacecraft of low-frequency electromagnetic fluctuations on kinetic scales embedded within fast flows in the Earth's plasma sheet. These fluctuations can generally be described as KAWs, which are continually radiated outward from the flow toward the auroral oval, low-latitude boundary layer or lobes.

Previously, *Swift and Lin* [2001] and *Lin and Swift* [2002] carried out a two-dimensional (2-D) global hybrid simulation for the nightside alone, which showed the generation of filamentary currents carried by Alfvén waves characteristic of the discrete aurora, due to the plasma turbulence generated by the breaking of fast earthward flows. In the near-Earth reconnection, accelerated ion beams are pitch angle scattered and trapped in large-amplitude Alfvén waves [*Hong et al.*, 2008]. Nevertheless, spatial variations and wave propagations in the east-west direction, which are important in a magnetospheric substorm, are missing in this 2-D model. A 3-D model is necessary to understand the nonlinear global physics, magnetotail waves, and the associated ion acceleration/heating and injection. Three-dimensional global hybrid models [*Karimabadi et al.*, 2006] can be a powerful approach to address the global kinetic physics.

In this paper, the fully kinetic ion dynamics in the magnetotail is investigated with a 3-D global hybrid simulation model for the first time. Both dayside and nightside are included in the calculation so that the global boundary condition is self-consistent and the global convection is also self-consistently included. The simulation is driven by a southward IMF, similar to the cases explored in observation by [*Angelopoulos et al.*, 2013]. Processes associated with ion injection to the inner magnetosphere are studied. The initial results are presented with a focus on the structure and evolution of the near-Earth plasma sheet and the transition region between the tail and the ring current region.

The outline of this manuscript is as follows. The global hybrid model is described in section 2. The simulation results are presented in section 3. A summary and discussion is given in section 4.

2. Simulation Model

The 3-D global hybrid code used in this study is developed by extending a previous version of the code that contains only the dayside magnetosphere [*Swift*, 1996; *Lin and Wang*, 2005] to include the nightside. The approach is different from the model of *Karimabadi et al.* [2006] based on a specialized multiscale technique. Our simulation domain includes the plasma region, in the GSM coordinate system, from $x = +20\ R_E$ on the dayside to $x = -60\ R_E$ on the nightside, $y = -30\ R_E$ to $+30\ R_E$ in the dawn-dusk direction, and $z = -30\ R_E$ to $+30\ R_E$ in the north-south direction. An inner boundary is assumed at the geocentric distance of $r \simeq 3.5\ R_E$. The Cartesian coordinate system is used in the calculation, in which this inner boundary is composed of a zigzag grid line approximating the spherical surface as in global MHD simulations [*Raeder et al.*, 1995]. In the hybrid code, the ions (protons) are treated as discrete, fully kinetic particles, and the electrons are treated as a massless fluid. Quasi charge neutrality is assumed.

The equation for ion particle motion, in the simulation units, is given as

$$\frac{d\mathbf{v}_p}{dt} = \mathbf{E} + \mathbf{v}_p \times \mathbf{B} - \nu(\mathbf{V}_p - \mathbf{V}_e), \tag{1}$$

where $\mathbf{v}_p$ is the ion particle velocity, $\mathbf{E}$ is the electric field, $\mathbf{B}$ is the magnetic field, ν is an ad hoc current-dependent collision frequency used to model the anomalous resistivity, with typical peak collision frequency ~ 0.01–$0.1\Omega_i$ [*Tan et al.*, 2011], and $\mathbf{V}_p$ and $\mathbf{V}_e$ are the bulk flow velocities of ions and electrons, respectively. For the region of the inner magnetosphere, a cold, incompressible ion fluid is assumed to be dominant in $r < 6\ R_E$, which coexists with particle ions [*Swift*, 1996; *Lin and Wang*, 2005], since our simulation focuses on the dynamics and ion kinetic physics in the outer magnetosphere. The number density of the cold ion fluid is assumed to be

$$N_f = (N_{\mathrm{eq}}/r^3)[1 - \tanh(r - 6.5)], \tag{2}$$

where r is in the unit of R_E, and $N_{\mathrm{eq}} = 1000$/c.c. when scaled to the real units, which is described later in this section.

The electric field is obtained from the massless electron momentum equation

$$\mathbf{E} = -\mathbf{V}_e \times \mathbf{B} - (1/N)\nabla p_e - \nu(\mathbf{V}_e - \mathbf{V}_i), \tag{3}$$

where $N = N_p + N_f$ is the total ion number density, N_p is the number density of discrete ions, and $\mathbf{V}_i = (N_p/N)\mathbf{V}_p + (N_f/N)\mathbf{V}_f$ is the total ion bulk flow velocity. The electron fluid is assumed to be isothermal, with a constant temperature T_e, and thus, $\nabla P_e = T_e \nabla N$. The electron flow speed is evaluated from Ampere's law,

$$\mathbf{V}_e = \mathbf{V}_i - \frac{\nabla \times \mathbf{B}}{\alpha N}, \tag{4}$$

where $\alpha = (4\pi e^2/m_i c^2)$, e is the electron charge, and m_i is the ion mass. Note that the constant α is related to the ion inertial length d_i as $d_i = 1/\sqrt{\alpha N}$. The choice of value of α sets the characteristic scale length d_i with respect to R_E in the simulation runs. The magnetic field is advanced in time following Faraday's law,

$$\frac{\partial \mathbf{B}}{\partial t} = -\nabla \times \mathbf{E}. \tag{5}$$

The numerical scheme is accurate to second order in both space and time. The code implements substepping loops for magnetic field update, which is mainly to maintain the numerical stability in the dipole high-field region and saves considerable computation time. The simulation is performed with a massively parallel computation approach.

The hybrid model is valid for low-frequency physics with $\omega \sim \Omega_i$ and $k\rho_i \sim 1$ (wavelength $\lambda \sim 6\rho_i$), where ω is the wave frequency, k is the wave number, Ω_i is the ion gyrofrequency, and ρ_i is the ion Larmor radius. For this range of wave frequency and wavelength, the ion kinetic physics in the near-Earth instabilities are resolved with grid sizes $\sim \rho_i$ or ion inertial length d_i. The finite ion gyroradius effects are resolved with particle time steps Δt much smaller than the gyroperiod.

In the case presented, the IMF $B_0 = 10$ nT, corresponding to a solar wind ion gyrofrequency $\Omega_0 = 0.958\ s^{-1}$. The solar wind ion inertial length $d_{i0} = c/\omega_{\mathrm{pi0}}$ is chosen to be 0.1 R_E. Since the peak ion number density in the plasma sheet is on the order of $0.1N_0$ [*Kivelson and Russell*, 1995], where N_0 is the solar wind ion number density; the ion inertial length in the tail is around 0.25 R_E–0.55 R_E in the simulation. Nonuniform cell grids are used, with a grid size of $(\Delta x, \Delta y, \Delta z) = (0.2\ R_E, 0.2\ R_E, 0.2\ R_E)$ in the near-Earth regions with $x \geq -20\ R_E$, $-12\ R_E \leq y \leq 12\ R_E$, and $-12\ R_E \leq z \leq 12\ R_E$ and a lower resolution in the lobes. The grid size Δx around the bow shock, magnetosheath, and magnetopause is reduced to 0.12 R_E, but the kinetic physics of magnetic reconnection in the dayside magnetopause may still not be resolved completely. These effects of the dayside kinetic structures are not emphasized in this initial study. The cell dimensions are chosen as $n_x \times n_y \times n_z = 300 \times 240 \times 240$. A total of 2×10^9 particles are used. A typical time step is $\Delta t = 0.05\Omega_0^{-1}$.

The initial condition includes the IMF (and solar wind ions) and a 3-D dipole field plus an image dipole. Ion particle density of 10% of the solar wind N_0 is assumed in the initial dipole field region, but most of these ions are lost from the tailside boundary as the field lines stretch out during the formation of the magnetotail.

The magnetosphere forms self-consistently by interaction between the solar wind and the geomagnetic field. The solar wind flows along the $-x$ direction from the frontside boundary at $x = 20\ R_E$, carrying the steady IMF. Outflow boundary conditions are used at the tailside boundaries $x = -60\ R_E$, $y = \pm 30\ R_E$, and $z = \pm 30\ R_E$. The inclusion of the cold ion fluid in the inner magnetosphere simplifies the conditions for the fluid-dominant low-altitude, inner boundary. A combination of spherical and Cartesian coordinates is used at the inner boundary. We let particles be reflected at exactly $r = 3.5\ R_E$. This simple reflection of the ion parallel velocity means that loss cone effects are omitted. For a particle distribution with an isotropic pitch angle distribution in a dipole field, the particles in a full loss cone are only one third of 1% of the total. Therefore, it seems reasonable to assume that the effect on the dynamics in this simulation is small. The **E** and **B** fields at the boundary reside on the Cartesian boundary approximating the spherical boundary, which are extrapolated to an extra grid point inside the $r = 3.5\ R_E$ surface. The **B** field is assumed to maintain the dipole field values at the inner boundary. The ionospheric conditions (1000 km altitude) are incorporated into the hybrid code, as in the existing global MHD models [*Raeder et al.*, 1995]. The field-aligned currents, calculated within the inner boundary, are mapped along the geomagnetic field lines into the ionosphere as input to the ionospheric potential equation

$$\nabla \cdot (-\boldsymbol{\Sigma} \cdot \nabla \Phi) = J_{\parallel} \sin I, \tag{6}$$

where Σ is the conductance tensor, Φ is the electric potential, $J_{\parallel}$ is the mapped field-aligned current density, and I is the inclination of the dipole field at the ionosphere. The static analytic model of Hall and Pederson conductance that accounts for EUV and diffuse auroral contributions [*Raeder et al.*, 1995; *Buzulukova et al.*, 2010] has been incorporated in the conductance tensor. In this paper, however, in order to contrast the results with the previous MHD calculations [*Mobarry et al.*, 1996], a uniform Pederson conductance, or the height-integrated conductivity, $\Sigma_P = 5$ (Siemens) is used, while the Hall conductance Σ_H is assumed to be zero. Therefore, $\nabla^2 \Phi = J_{\parallel}/\Sigma_P$ [*Mobarry et al.*, 1996]. The results in this paper correspond to a simplified model of ionospheric conductivity.

The local physics is scaled with the local ion inertial length d_i (or ρ_i) and the Alfvén speed V_A. The global size of the bow shock and the magnetopause (e.g., its standoff distance R_{MP}), on the other hand, is determined by the Mach number and the geomagnetic dipole strength. In the present simulation, the Mach number, ion β_i value, and the dipole field strength all have the realistic values, but the ratio d_{i0}/R_{MP} is larger than the realistic value in order to accommodate to the computation resource. In some other existing global hybrid simulations of the Earth's magnetosphere, the dipole field strength is assumed to be smaller than that in reality while d_{i0} is kept at the realistic value, which also corresponds to a similar unrealistic d_{i0}/R_{MP} for the magnetosphere [*Blanco-Cano et al.*, 2009]. The scaling study of *Omidi et al.* [2006] shows that Earth-like magnetosphere appears when $R_{\mathrm{MP}}/d_{i0} < 0.05$. In the present simulation, $R_{\mathrm{MP}}/d_{i0} \simeq 0.01$.

Due to the necessity of using an artificial solar wind ion inertial length, d_{i0}, it is necessary to scale the kinetic effects in order to compare with typical values in the magnetosphere. For an ordinary solar wind density of 6/c.c., the value of the solar wind ion inertial length is 0.0148 R_E, a factor of 6.77 smaller than the value of d_{i0} used in the simulation. Because time is scaled by a realistic value of the inverse of the solar wind ion gyrofrequency Ω_{i0}, the Alfvén speed, $V_{A0} = d_{i0}\Omega_{i0}$, must be larger too. Thus, convection speed is faster in the simulation. Therefore, while the macroscopic distances, e.g., position of the bow shock and magnetopause, are realistic, the kinetic effects are larger than they would be in reality. In contrast, the global times in the simulation are shorter by the same factor. So in order to make a direct comparison with realistic global convection times, the global times presented are increased by the factor 6.77. In the presentation below, the spatial length is in units of R_E and the velocity in km/s. The magnetic field is in units of nT and the temperature in units of eV. The ion number density is in units of /c.c. as scaled to the realistic ion inertial length.

3. Simulation Results

We show a case driven by a constant IMF that points purely southward, with an Alfvén Mach number $M_A = 7.87$. The IMF components $B_{x0} = B_{y0} = 0$, and $B_{z0} = -10$ nT. Corresponding to ion density $N_0 = 6$/c.c., the solar wind convection speed is set to be $V_0 = 700$ km/s, the ion temperature is $T_{i0} = 10$ eV, and electron-to-ion temperature radio $T_{e0}/T_{i0} = 0.1$

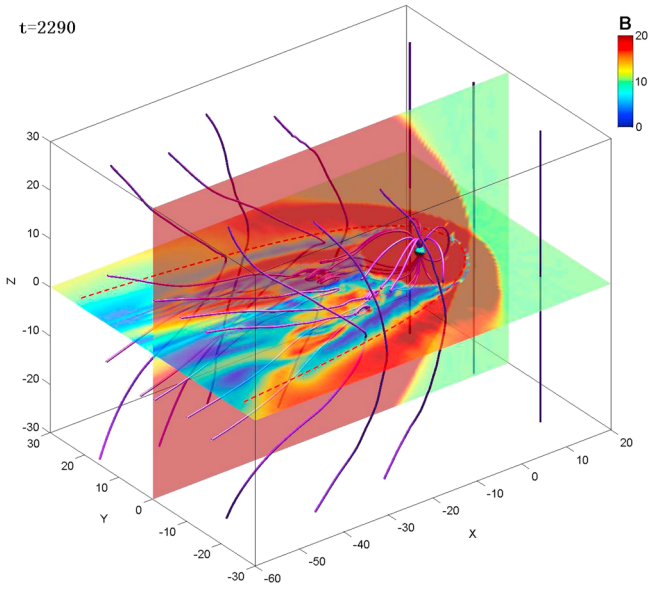

Figure 1. Magnetic field lines and contours of the field strength B at the $z = 0$ (equatorial) plane and the $y = 0$ (noon-midnight meridian) plane at $t = 2290$ s.

3.1. Magnetotail Reconnection

Figure 1 shows the magnetic field lines in the 3-D perspective as well as contours of the field strength B in the $z = 0$ (equatorial) and $y = 0$ (noon-midnight meridian) planes at $t = 2290$ s. The magnetosheath field is predominantly in the southward direction under the southward IMF. These field lines are reconnected with the northward geomagnetic field at the magnetopause on the dayside. The red dashed line in Figure 1 marks the approximate shape and location of the magnetopause, which for illustration purpose is fitted with [*Shue et al.*, 1997]

$$r_{MP} = r_0 \left(\frac{2}{1 + \cos\phi} \right)^{\alpha}, \qquad (7)$$

where $r_0 \sim 7.5\ R_E$ is the standoff distance of the magnetopause at the subsolar point, $\alpha = 0.65$, and ϕ is the longitudinal angle measure with respect to the x axis. Reconnection X lines are generated at the magnetopause, not shown in this figure, with the presence of dominant X lines from the nose through the entire dayside local times and flux ropes associated with flux transfer events, similar to those in the 3-D dayside global hybrid simulation of *Tan et al.* [2011]. The dayside reconnection begins at $t \simeq 180$ s. The reconnection electric field $E_y \sim 4$ mV/m on the dayside penetrates into the lobes through the opened magnetopause, resulting in a dawn-dusk $E_y \simeq 2$–3 mV/m in the tail. A thinning of the tail plasma sheet [*Swift and Lin*, 2001] is driven subsequently, corresponding to the growth phase of substorm, and then magnetic reconnection occurs at $t \simeq 1245$ s in the plasma sheet. The tail reconnection first takes place around $x \simeq -20\ R_E$ where the current sheet is the thinnest and is found to be highly 3-D, with X line lengths $\sim 1\ R_E$–$10\ R_E$. The reconnection flux ropes at $t = 2290$ s can be seen in Figure 1 from $x = -15\ R_E$ to $-30\ R_E$, corresponding to multiple X lines. Remarkable variations are shown in the B field strength at $z = 0$ due to the wavy motion or flapping of the current sheet, where the low field, in general, indicates the center of the sheet and/or the location of the reconnection X lines.

To illustrate reconnection in the magnetotail, Figures 2a–2f show, in turn, the structure of field strength B, ion density N, dawn-dusk magnetic field component B_y, Sun-Earth component of ion flow velocity V_{ix}, and the electric field components E_x and E_z from $x = -40\ R_E$ to $-10\ R_E$ in the xz plane along $y = 0$ at $t = 2505$ s. Some typical field lines traced in the 3-D space are also drawn in each plot. In Figure 2a the thin current sheet, which can be seen around $z \simeq 0$ where the B field has a minimum and the field direction reverses, has a half width $\simeq 0.5\ R_E \simeq 1.4 d_i$ at the thinnest areas near the X lines, where $d_i \simeq 0.365\ R_E$ is the ambient ion inertial length. Note that $\beta_i \sim 0.08$ in the ambient plasma. Our grid size is enough to resolve the ion kinetic physics, as seen from previous hybrid simulations [*Krauss-Varban and Omidi*, 1995; *Lin and Swift*, 1996; *Scholer and Lottermoser*, 1998; *Karimabadi et al.*, 1999]. An X line is located at $x \simeq -27\ R_E$ in the current sheet at $y = 0$. Our method of identification of X lines for the tail current sheet is the same as that described by *Tan et al.* [2011] and consistent with the general procedure described by *Priest and Forbes* [2000]. When an X line that separates local areas of four different types of magnetic connectivity exists, the X type configuration of field lines can be located when mapping the 3-D field lines into an xz reference plane. The point of the X line in the plane is marked by a dot in Figure 2. An X line segment can be traced by connecting the X points in a series of such planes. Other supporting evidence of the X line is discussed below, such as the existence of opposite flow jets and quadrupole out-of-plane magnetic field and the corresponding electric field structure. Figure 2b shows that the ion density increases from ~ 0.5/c.c. to 1.0/c.c. across the separatrix of reconnection, while the lobe density is as low as 0.2–0.5/c.c. On the earthward side of this X line, there exists another X line around $x \simeq -18\ R_E$, due to the convection of the reconnected field lines from an earlier time. A flux rope has formed between these two X lines. (See the density peak in Figure 2b at $x \simeq -21\ R_E$.)

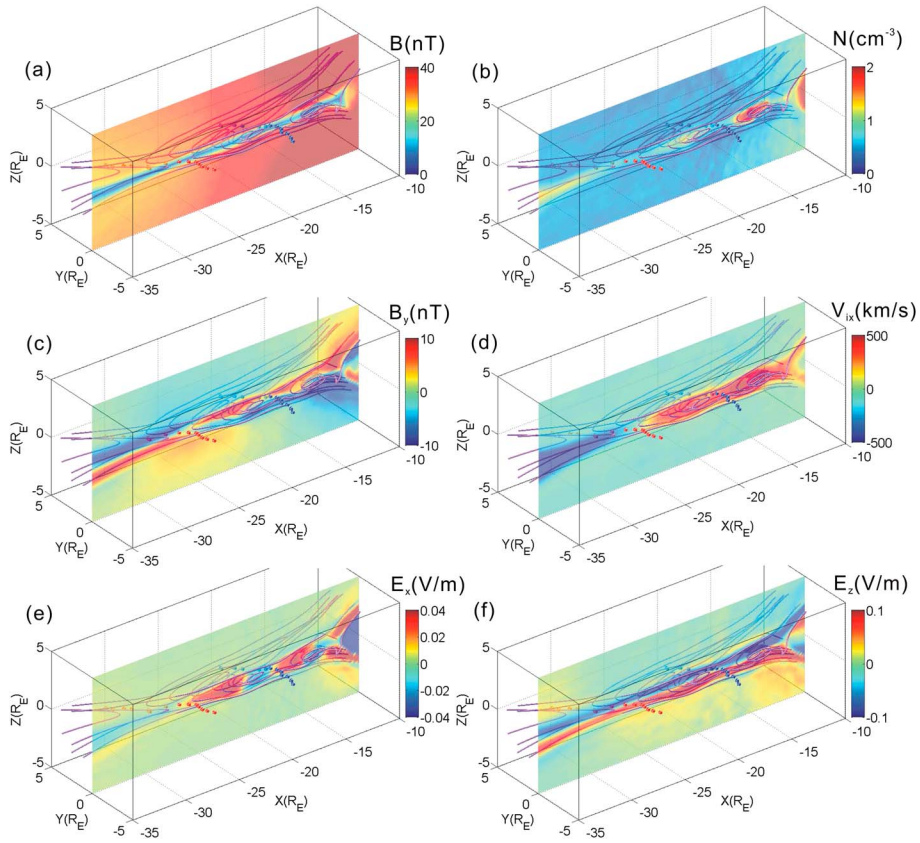

Figure 2. Structure of (a) field strength B, (b) ion density N, (c) dawn-dusk magnetic field component B_y, (d) Sun-Earth component of ion flow velocity V_{ix}, (e) electric field component E_x, and (f) E_z from $x = -40\ R_E$ to $-10\ R_E$ in the xz plane along $y = 0$ at $t = 2505$ s, with projected field lines.

A larger density $\simeq$ 2.0/c.c. is centered at $x \simeq -15\ R_E$ due to another flux rope that has propagated closer to the Earth. The quadrupolar structure of B_y around the X line at $x \simeq -27\ R_E$ (see Figure 2c) clearly exhibits a signature of the Hall effects associated with the fast reconnection. This ion inertial effect [*Sonnerup*, 1979; *Terasawa*, 1983; *Drake*, 1995] is self-consistently resolved in the hybrid model, and the corresponding charge separation effect leads to an $E_x > 0$ on the earthward side of the X line and $E_x < 0$ on the tailward side (see Figure 2e), following

$$\mathbf{E}_{\text{Hall}} = \mathbf{J}_e \times \mathbf{B}/N, \tag{8}$$

where $J_e \simeq J_e e_y$ is the electron cross-tail current. The positive E_x is more pronounced because of a larger reconnection magnetic field B_z on the earthward side. A similar E_x structure is also seen around the X line at $x \simeq -18\ R_E$. The Hall effects are shown in the E_z component as well, with $E_z < 0$ northward of the current sheet and $E_z > 0$ southward (see Figure 2f). The structure of the magnetic field is consistent with that of a nearly zero guide field, in which a quadrupolar B_y structure is dominant [*Drake*, 1995]. A core field with a magnitude nearly equal to the solar wind B_0 is also generated inside some flux ropes, whereas in other flux ropes there is no obvious core field. The generation mechanism of the core field and its relation to the ambient guide field [*Karimabadi et al.*, 1999], as well as the detailed physics of the 3-D reconnection, will be discussed in a separate paper.

Bidirectional ion acceleration is observed on the two sides of the X line around $x \simeq -27\ R_E$, as seen from Figure 2d. The stronger reconnection at this location dominates the flow pattern in the mid- and near tail. As a result, high-speed bulk flows up to $\sim$ 600 km/s are shown in V_{ix} due to the ion $\mathbf{E}\times\mathbf{B}$ drift associated with the reconnection electric field $E_y > 0$. The V_{ix} flow is earthward for $x > -25\ R_E$, resulting in the ion injection to the inner magnetosphere. As the time proceeds, multiple reconnection X lines and thus flux ropes continuously form from the tail plasma sheet. Correspondingly, the reconnected flux ropes are convected toward the inner magnetosphere.

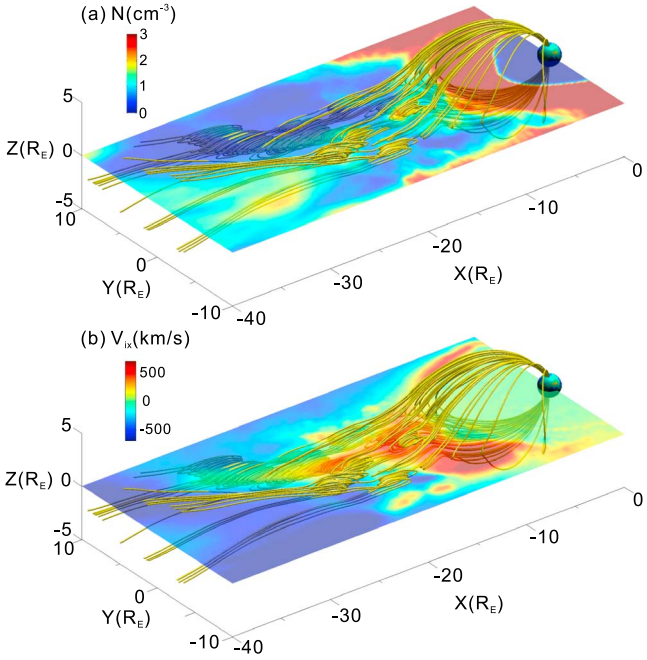

Figure 3. Contours of (a) N, ion bulk flow component (b) V_{ix}, and magnetic field lines in the zoomed near-tail region of the equatorial ($z = 0$) plane at $t = 2505$ s.

3.2. Dawn-Dusk Asymmetry of the Plasma Sheet

The Hall electric field E_z shown in Figure 2f is present even before the magnetotail reconnection takes place. The ion inertial effects show up when the half width of the tail current sheet is thinned to about 8 times the ion inertial length d_i, at $t > 1290$ s. With the presence of this electric field E_z, the ions gain a dawnward (in the $-y$ direction) $\mathbf{E} \times \mathbf{B}$ drift velocity, associated with E_z and B_x, both northward and southward of the current sheet center everywhere along the thinned plasma sheet. The magnetic curvature and gradient drifts in the plasma sheet, on the other hand, are negligible. A systematic dawnward particle drift is therefore present in the plasma sheet. The electron density changes in the same ways as the ion density through the quasi-charge neutrality condition.

The Hall effects become stronger after the onset of reconnection, with the presence of the Hall E_x field due to the finite B_z. Since the Hall E_x field is positive (negative) at the locations where $B_z > 0$ ($B_z < 0$), the ion $\mathbf{E}_x \times \mathbf{B}_z$ drift velocity also always points to the $-y$ (dawnward) direction. Nevertheless, unmagnetized ions in the thin boundary layer of reconnection are accelerated by the reconnection field E_y, which points to the $+y$ direction together with the magnetic drifts. The dawnward drift motion is therefore weakened. The dominant ion acceleration in reconnection is in the x direction due to the E_y, and the ion bulk flow is dominated by V_{ix}.

As a result of the dawnward particle drift, the plasma density in the plasma sheet is smaller on the duskside than the dawnside. Overall, the thinner plasma sheet on the duskside allows for more frequent triggering of reconnection. Figure 3 depicts contours of the ion density N and V_{ix} flow velocity in the zoomed mid- to near-tail regions of the equatorial ($z = 0$) plane at $t = 2505$ s. Superposed on each plot are the magnetic field lines. Lower density, comparable to the solar wind value of approximately 0.5/c.c., is seen on the $y > 0$ (dusk) side, whereas it is around or above 1.0/c.c. on the $y < 0$ side. Correspondingly, more reconnection flux ropes are present on the $y > 0$ side (not all are shown in Figure 3). Trapped ions are seen in the flux ropes, as shown in the density plot. A similar filamentary density structure was found in the flux ropes obtained in the hybrid simulation of the dayside magnetopause [*Tan et al.*, 2011].

The dawn-dusk asymmetry in the global distribution of the magnetotail reconnection results in stronger high-speed flows on the duskside than on the dawnside and therefore a stronger flow injection toward the inner magnetosphere ($V_{ix} > 0$) on the duskside, as seen in Figure 3b. The magnitude of the flow speed is $V_{ix} \sim 500$ s, while the flow direction is oblique toward $-y$. As the ions are injected toward the inner magnetosphere, the flow then diverges around the strong dipole field obstacle. The ions that are injected deeper into the dipole region gain a westward ($V_{iy} > 0$) speed around $r = 10\ R_E$ due to the magnetic gradient and curvature drift in the dipole-like field region, which is discussed later. Overall, the ions undergo a dawnward drift in the tail and then a duskward/westward drift in the ring current region. Note that the ring current particles in the simulation are mainly from the transmitted solar wind ions. The dawn-dusk asymmetry in the plasma sheet affects the near-Earth dynamics near the magnetic field dipolarization front and the ring current, which is shown later.

3.3. Ion Phase Space Distributions

Typical ion phase space properties in the magnetotail associated with the ion injection are shown in Figure 4. Plotted in Figure 4 are the distributions in the v_{px}-v_{py} plane (top row) and the v_{px}-v_{pz} plane (bottom

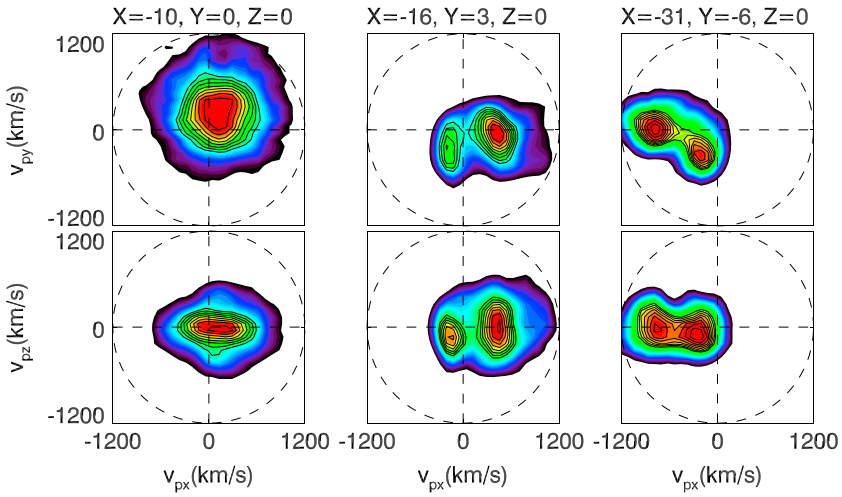

Figure 4. Typical ion distributions in (top row) the v_{px}-v_{py} plane and (bottom row) the v_{px}-v_{pz} plane are shown for $(x, y, z) = (-10.0, 0, 0)\ R_E$ in the ring current region, $(x, y, z) = (-16.0, 3.00, 0)\ R_E$ on the earthward side of the dominant X lines, and $(x, y, z) = (-31.0, -6.00, 0)\ R_E$ on the tailward side of the X lines.

row) at $t = 2505$ s, at three different locations: $(x, y, z) = (-10.0, 0, 0)\ R_E$ just behind the dipolarization front, $(x, y, z) = (-16.0, 3.00, 0)\ R_E$ on the earthward side of the dominant X lines, and $(x, y, z) = (-31.0, -6.00, 0)\ R_E$ on the tailward side of the X lines. The color contours are plotted on the logarithmic scales. A heated distribution is found at $(x, y, z) = (-10.0, 0, 0)\ R_E$, as seen in Figure 4 (left column), with the particle velocities centered at $(v_{px}, v_{py}, v_{pz}) \simeq (200, 250, 0)$ km/s. The heating is mainly in the direction perpendicular to the magnetic field, which points nearly to the z direction at this equatorial location. In the perpendicular plane, the ion distribution is nearly gyrotropic.

In the plasma sheet, the results reveal the presence of ion populations/beams due to magnetic reconnection. At $x = -16\ R_E$, an earthward accelerated hot ion beam is centered at $(v_{px}, v_{py}, v_{pz}) \simeq (400, 0, 0)$km/s, as seen in Figure 4 (middle column). This ion population coexists with a cold, pancake-shaped inflow (to the X line) of ions, which has central velocity components at $v_{px} \simeq -180$ km/s (see both panels), a duskward $v_{py} \simeq -250$ km/s (top), and a southward $v_{pz} \simeq -120$ km/s (bottom), while the current sheet center is slightly below $z = 0$. At $x = -31.0\ R_E$ tailward of the dominant X lines, an accelerated ion beam, centered at $v_{px} \simeq -900$ km/s, is ejected to the tailside. This ion beam coexists with another ion beam that is also moving tailward due to the existence of multiple X lines/magnetic islands.

Overall, the ion distributions are largely anisotropic. The ion temperature is enhanced in reconnection due to heating and parallel mixing of ion beams along field lines, consistent with previous simulation studies [*Lin and Swift*, 1996; *Kuznetsova et al.*, 1996]. The ion heating in the time-dependent collisionless reconnection has been found to be due to wave-particle interaction associated with Alfvén waves [*Lin and Swift*, 2002] or an ion pickup process in the Alfvénic outflow [*Drake et al.*, 2009]. Previous 2-D global hybrid simulations of *Swift and Lin* [2001] and *Hong et al.* [2008] have shown that wave turbulence behind the dipolarization front can lead to a strong ion heating. Our 3-D simulation shows that such heating is mainly in the direction perpendicular to the **B** field. It is also found from our simulation that farther behind the dipolarization front into the dipole-like magnetic field, the heated distribution becomes isotropic. The dynamic structure of the near-Earth tail and the resulting waves are discussed below.

3.4. Dynamic Evolution of the Dipolarization Front

To examine the dynamic evolution of the near-Earth magnetotail associated with the ion injection, Figure 5 shows contours of N, B, B_x, ion flow component V_{ix}, cross-tail current density J_y, and the perpendicular ion pressure $P_\perp$ in the equatorial ($z = 0$) plane, from $x = -20\ R_E$ to $12\ R_E$, in a time sequence of $t = 1432$ s, 1861 s, 2505 s, and 2863 s. At the early time $t = 1432$ s, the bow shock can be seen at a standoff distance of $r = 11.5\ R_E$, across which B, N, and the pressure $P_\perp$ increase in the antisunward direction (see Figures 5a, 5e, and 5u). On the dayside, the thin layer of large perpendicular current J_y and low B field strength through the standoff distance of $7.5\ R_E$ marks the magnetopause (see Figures 5e and 5q). The dayside reconnection has caused the direct transport of magnetosheath ions to the open low-latitude boundary layer (LLBL) just

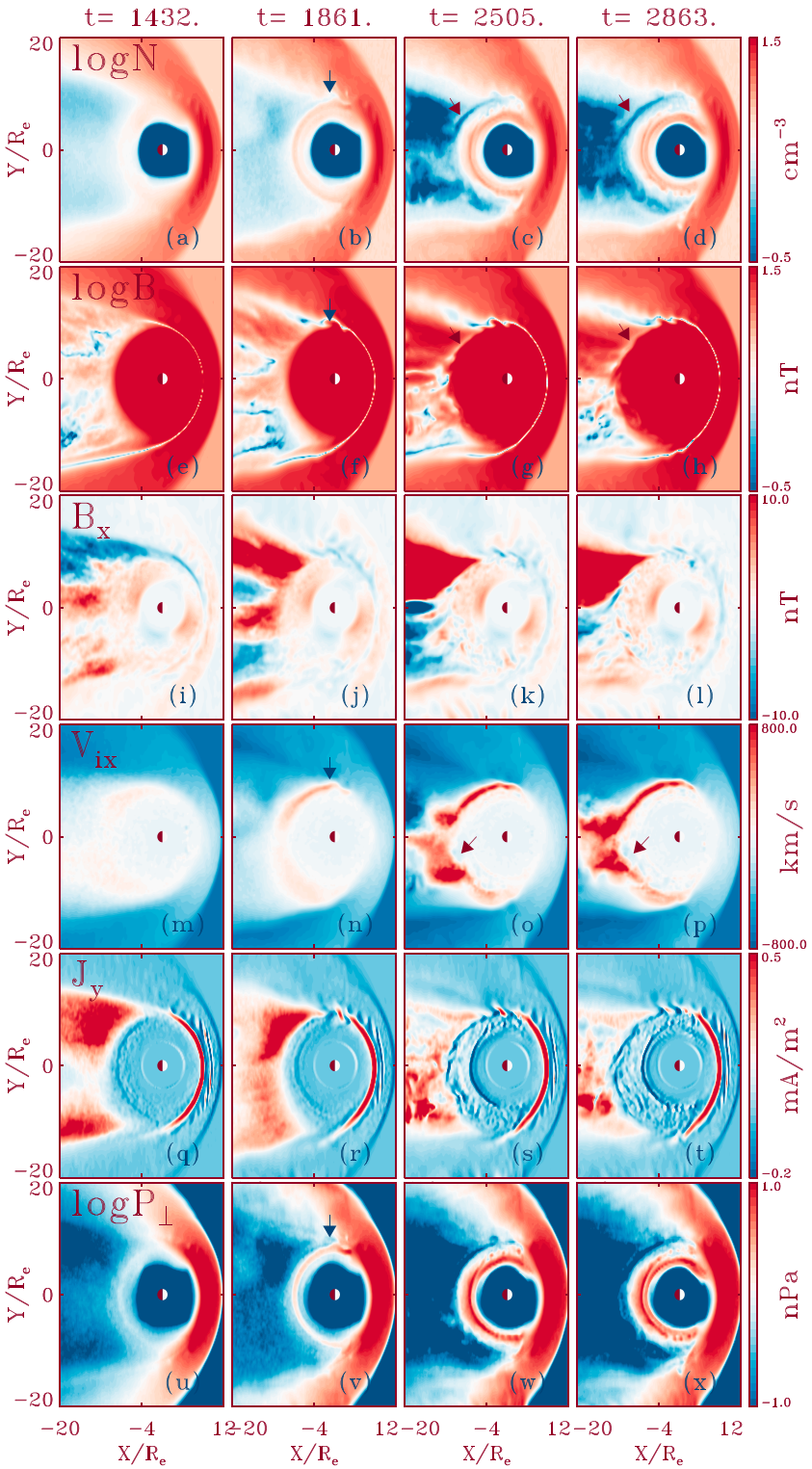

Figure 5. Contours of *N*, *B*, B_x, V_{ix}, cross-tail current density J_y, and the perpendicular ion pressure $P_\perp$ in the equatorial ($z = 0$) plane in a time sequence of $t = 1432$ s, 1861 s, 2505 s, and 2863 s show the dynamic evolution of the near-Earth magnetotail around the dipolariztion front and ring current region. The dark blue arrows indicate vortex ripples due to a shear flow-type instability. The dark red arrows in the plots of *B* and *N* mark the dip-B structure at the dipolarization front, and the dark red arrows in the V_{ix} plots indicate the reversal of the flow.

inside the magnetopause (see Figure 5a). On the tailside, the plasma sheet is thinned but still quiet (not visible in this view), with a lower density on the duskside than the dawnside, as discussed above. The cross-tail currents, with $J_y > 0$, are stronger on the duskside where the plasma sheet is thinned more significantly due to the lower density (see Figure 5q). The sheet center on the duskside is slightly above the $z = 0$ plane (not visible in this figure), where $B_x < 0$ is observed, while the sheet center on the dawnside is slightly below $z = 0$. At this moment, X lines have just formed around $x \simeq -20\ R_E$. Little ion earthward injection is present in this early stage of the magnetotail reconnection, as seen from the small $V_{ix} < 100$ km/s and small $P_\perp$ in the near-tail (see Figures 5m and 5u).

The effects of the tail reconnection are significant at $t = 1861$ s, while the reconnection flux tubes propagate toward the Earth with the earthward flow convection. The taillike field is connected to the dipole-like field at $x \simeq -10\ R_E$, as seen from the abrupt increase of B and decrease of B_x earthward of $x = -10\ R_E$ (see Figures 5f and 5j). The earthward ion injection from the tail reconnection has caused the accumulation of ions in the dipole field region, forming an apparent ring of density N and pressure $P_\perp$ around $r \leq 8\ R_E$ (see Figures 5b and 5v). These are the ring current ions that originated from the transmitted solar wind particles. The earthward ion bulk flow diverges around the region with the piled up magnetic field and pressure, as seen from the enhanced V_{ix} outside the ring current. There also exists a dawn-dusk asymmetry in the ion flow component V_{ix} at the outer edge of the ring (see Figure 5n). On the duskside, the westward direction of the ion magnetic gradient and curvature drifts is consistent with the ion flow direction. The earthward V_{ix} is weaker at the dawnside edge because there the westward/tailward gradient/curvature drifts reduces the net earthward V_{ix}.

Meanwhile, the dayside reconnection drives the tailward convection of the transmitted magnetosheath plasma in the LLBL, from the subsolar region to the flanks. Around the duskside termination line ($x = 0$), this tailward convection encounters the westward/sunward drift of the ring current ions from the magnetotail, generating a shear flow-type instability, which is evident from the vortex ripples in B, ion density N, V_{ix}, and $P_\perp$ around $(x, y) = (0, 9.0\ R_E)$ (see the dark blue arrows in Figures 5b, 5f, 5n, and 5v). The perpendicular current J_y breaks into large $k_\perp$ structures. On the dawnside, however, the shear flow instability is significantly weaker.

At $t = 2505$ s, high-speed earthward flows of $V_{ix} \sim 700$ km/s are present in the mid- to near-tail regions, again outside the ring current (see Figure 5o). The ring current density is significantly enhanced due to the continuous ion injection from the tail, to 8/c.c., and the pressure $P_\perp$ is also built up (see Figures 5c and 5w). The pressure ring is thinner on the dawnside than at midnight and on the duskside. The ring current ions have occupied a broader region, from $r \simeq 5\ R_E$ to $9\ R_E$ (see Figure 5c). The dipole-like high-field region has expanded tailward because of the continued earthward ion injection and field pileup, compared with the earlier times (compare Figures 5f and 5g). The front of such "dipolarization" of the taillike field lines propagates tailward with time. At $t = 2505$ s, the dipolarization front is located around $x = -12\ R_E$ along the Sun-Earth line, where the magnitude of the x component magnetic field, $|B_x|$, suddenly decreases (see Figure 5k).

The earthward ion flow V_{ix} is stopped abruptly at the dipolarization front. Immediately earthward of this flow breaking, the ion V_{ix} is reversed in the dawnside ring current where the eastward moving ions of the tail are turned westward at the edge of the dipole-like field region. The presence of the negative V_{ix} is indicated by the dark red arrow in the V_{ix} in Figure 5o, where V_{ix} has just turned from positive values in the plasma sheet to negative behind the dipolarization front. Oscillations of the dipolarization front are generated, with a larger amplitude on the dawnside. At the dipolarization front, strong turbulence in the magnetic field and density is generated, which propagates eastward and westward in the azimuthal direction (see Figure 5k). A thin layer with a sharp dip in B is present at the duskside front, as indicated by the dark red arrow in Figure 5g, in front of the sharp rise of the magnetic field. The presence of the dip in B at the dipolarization front has been reported in satellite observations [*Runov et al.*, 2009] and attributed to the reflected ions at the front [*Zhou et al.*, 2014]. In Figure 5g, the thickness of the dip in B layer is $\simeq 0.2\ R_E$, which is approximately the local ion Larmor radius ρ_i. The ion density peaks in the thin layer (indicated by the dark red arrow in the density plot, Figure 5c) due to the ion trapping. No temperature enhancement is found. The current J_y breaks into small-scale structures with larger wave number $k_\perp \rho_i \sim 1$ around the ring current and the plasma sheet (see Figure 5s).

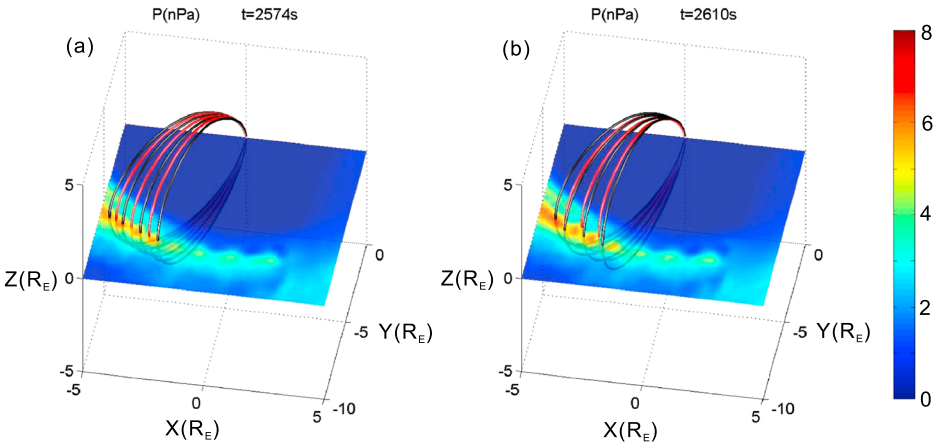

Figure 6. Structure of ion pressure P at (a) $t = 2574$ s and (b) 2610 s in the dawnside equatorial plane around the ring current. Motion of some typical magnetic field lines going through the ring current is traced.

At $t = 2863$ s, B_x in the near tail is further reduced, but the location of the dipolarization front happens to be similar to that at $t = 2505$ s as the front oscillates with time. The dip in B and the corresponding density peak are again marked by dark red arrows (see Figures 5d and 5h). The reversal of V_{ix}, indicated by the dark red arrow in the velocity plot, remains dominant on the dawnside (see Figure 5p). While the shear flow instability dominates the dusk ring current, breakup of ring current ion pressure is also observed on the dawnside flank, around $r = 7.5$ and $x > -5\ R_E$. The breakup and associated ion transport is due to the kinetic ballooning-type instability.

3.5. Presence of Kinetic Ballooning Instability

Figure 6 depicts the zoomed-in structure of ion pressure P in the dawnside equatorial plane at $t = 2574$ s and 2610 s. Motion of some typical magnetic field lines going through the ring current is tracked by following the electron flow elements that are nearly frozen to the field lines. Interchange motion of the field lines is shown by the relative motion of the red and black field lines at these two times. Correspondingly, finger-like structures [*Pritchett and Coroniti*, 2010], with the dominant wave vector **k** in the azimuthal direction and $k_\perp \rho_i \sim 0.46$–0.71, are seen in the plasma pressure. The ion beta value is estimated to be $\beta_i \simeq 3.4$. The unstable "fingers" grow in the radial direction, resulting in a radial ion transport.

The time evolution of the amplitude of the perpendicular ion pressure $P_\perp$ in the finger-like structure is illustrated in Figure 7, where the dashed line shows an exponential fit to the growth stage, $\Delta P_\perp \sim \exp(\gamma_{\rm sim} t')$, with the fitted growth rate $\gamma_{\rm sim} \simeq 1.35\Omega_i$, where Ω_i is the local ion gyrofrequency, the time $t' = t - t_0$, and $t_0 = 2502$s is the time when the instability starts to grow. The exponential growth is seen in $\Omega_i t' < 2.8$, and the growth is gradually saturated at $\Omega_i t' > 2.8$. Based on the analytical theory of *Cheng and Lui* [1998], the linear dispersion relation of kinetic ballooning instability can be written as

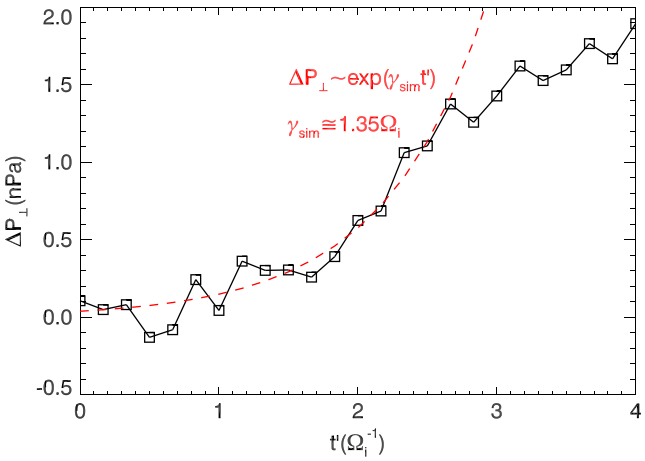

Figure 7. Growth of the amplitude of the ion perpendicular ion pressure in the finger-like structure shown in Figure 6. The dashed line shows an exponential fit, with the fitted growth rate obtained from the simulation $\gamma_{\rm sim} \simeq 1.35\Omega_i$.

$$\omega(\omega - \omega_{*\rm pi}) = (1 + b_i)V_A^2 S k_\parallel^2 - (1 + b_i)V_A^2 \frac{2\mu_0 \kappa \cdot \nabla P}{B^2}, \quad (9)$$

where $\omega_{*\rm pi} = (\mathbf{B} \times \nabla P) \cdot \frac{v_{\rm thi}^2 \mathbf{k}_\perp}{B\Omega_i P}$, $v_{\rm thi}$ is the ion thermal speed, $S = 1 + \frac{b_i}{(1+b_i)} \frac{T_e}{T_i}$ in this simulation without the trapped electrons, $b_i = \frac{1}{2} k_\perp^2 \rho_i^2$, and κ is the magnetic

curvature. The solution of the instability is then obtained as

$$\omega = \omega_r + i\gamma_{\text{th}}, \tag{10}$$

with the real frequency

$$\omega_r = \frac{1}{2}\omega_{*\text{pi}} \simeq \frac{1}{2}(k_\perp \rho_i)\Omega_i \left(\frac{\rho_i}{L_p}\right)\left(\frac{\Delta P}{P}\right), \tag{11}$$

where L_p is the characteristic scale length of the pressure gradient. Let $\alpha \equiv -(1+b_i)V_A^2 S k_\parallel^2 + (1+b_i)V_A^2 \frac{2\mu_0 \kappa \cdot \nabla P}{B^2}$. The theoretically predicted growth rate is

$$\gamma_{\text{th}} = \frac{1}{2}\sqrt{\omega_{*\text{pi}}^2 - 4\alpha} \simeq \sqrt{\beta_i(1+b_i)\left(\frac{V_A^2}{R_c L_p}\right)\frac{\Delta P}{P} - (1+b_i)S k_\parallel^2 V_A^2 - \omega_r^2}, \tag{12}$$

where R_c is the magnetic curvature radius. For $k_\perp \rho_i \simeq 0.71$, $\Delta P/P \simeq 0.6$ with $L_p \simeq 1\ R_E = 6370$ km, $\rho_i/L_p \simeq 0.11$, $V_A^2/(R_c L_p) \simeq 0.063$, $\lambda_\parallel \simeq (4\ R_E)\pi$, $T_e/T_i \sim 0.1$, and $\beta_i \simeq 3.4$ as measured in the simulation for the region with the instability, the real frequency is estimated as $\omega \simeq 0.024\Omega_i$ and the growth rate $\gamma_{\text{th}} \simeq 1.43\Omega_i$ based on the analytical theory. The frequency obtained in the simulation is found to be consistent with the theory, and the growth rate $\gamma_{\text{sim}} \sim 1.35\Omega_i$ is also close to the analytical γ_{th}. Note that in the above estimate of the instability, we have used the local V_A and v_{thi} in the simulation unit of velocities without the global scaling. In this case, the threshold ion β_i for the occurrence of ballooning instability can be estimated as $\beta_c \simeq \frac{\omega_{*\text{pi}}^2 R_c L_p}{4(1+b_i)V_A^2} + S\left(L_p R_c k_\parallel^2\right) \simeq 1.26$ based on the analytical theory.

In this simulation, the ballooning instability takes place on the dawnside, while no such instability is seen at midnight, different from the instability observed prior to dipolarizations by *Saito et al.* [2008]. The scale lengths L_p and R_c at midnight are slightly larger than those at the dawn flank. Based on the plasma and magnetic field conditions at midnight, the linear growth rate of ballooning instability can be estimated as nearly 50% of the above γ_{th} at the dawnside. The ballooning instability at midnight may be too weak and overwhelmed by the compressional wave turbulence at midnight due to the direct impacts of BBFs. Recall that the convection speed used in the simulation is larger than that in reality. As a result, the faster pressure buildup and subsequent development of turbulence at midnight may have further diminished the appearance of the ballooning structures, if they exist. At the dawnside, however, the plasma is quiet.

3.6. Propagation of Compressional and Alfvén Mode Waves

Azimuthal propagation of the kinetic compressional waves near the dipolarization front is shown in Figure 8 for B, V_x, and $P_\perp$ versus the azimuthal angle ϕ along the ring current from $r = 10\ R_E$ at the midnight angle $\phi = 180°$, in a time sequence from $t = 2000$ s to 2800 s. The angle $\phi = 90°$ denotes the duskside termination line $x = 0$. The wave perturbations are of broadband nature. The impinging and impact of fast flows from the tail reconnection can be seen from the large-amplitude and global size V_{ix} perturbations, which propagate outward with a speed of ~80 km/s to the flanks at this location behind the dipolarization front. On top of the large-scale perturbations, ion kinetic-scale compressional waves propagate away from the near-midnight area, with an in-phase oscillation between B and $P_\perp$. These compressional waves are seen more clearly on the dawnside. Their propagation speed is ~500 km/s. The large-amplitude staged waves on the duskside, near $\phi = 90°$–$100°$, are those due to the shear flow instability.

Similar to the previous 2-D global hybrid simulations [*Lin and Swift*, 2002; *Hong et al.*, 2008], shear Alfvén waves are found to be generated in the plasma sheet boundary layer from the magnetotail reconnection, together with compressional waves. To illustrate the structure associated with the field-aligned Alfvénic propagation, Figure 9 shows contours of V_{ix}, B_y, the y component ion flow velocity V_{iy}, and the parallel current $J_\parallel$ in the noon-midnight meridian plane, $y = 0$, at $t = 1797$ s (left column) and 2863 s (right column). At $t = 1797$ s, a reconnection X line exists at $x \simeq -18\ R_E$. Bidirectional V_{ix} flows are generated from reconnection. The presence of large-amplitude Alfvén waves in reconnection can be identified by the correlated perturbations in the transverse components B_y (due to the ion inertial effects) and V_{iy} (more obvious at the later time $t = 2863$ s), as well as the associated $J_\parallel$. These Alfvén modes originated from the X line with wave vector roughly normal to the current sheet, forming an elongated wavefront ($k \simeq k_z$, with scale length ~ 2–3d_i) while the wave structures are carried away by the convection.

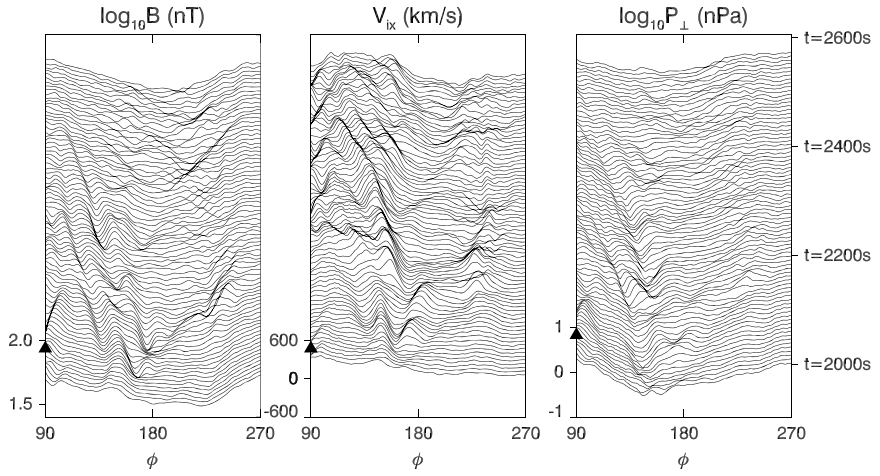

Figure 8. Quantities B, V_x, and $P_\perp$ versus the azimuthal angle ϕ along the equatorial path $x^2/a^2 + y^2/b^2 = 1$, with $a = 10\ R_E$ and $b = 8.5\ R_E$, roughly following the ring of the ring current, in a time sequence from $t = 2000$ s to 2800 s. At the duskside termination line $x = 0$ is $\phi = 90°$.

At the later time $t = 2863$ s, the existence of multiple X lines (two are seen at $x = -20\ R_E$ and $-32\ R_E$ in this plane) leads to a highly 3-D Alfvén wave structure in the plasma sheet. Note that these reconnection events are not the same ones at the earlier time $t = 1797$ s. The interaction between the multiple X lines in the tail results in mixed polarities of the field and flow, as seen in Figure 9 (right column). Meanwhile, compressional waves in B and N are also generated from the plasma sheet and the dipolarization front, as discussed above. Figure 10a shows the detailed structures of V_{iy} and V_{Ay}, the y component Alfvén velocity, along the line segment S_1 indicated in the V_{iy} plot in Figure 9 (right column) from $z = -5.0\ R_E$ to $+5.0\ R_E$ at $x = -12.0\ R_E$, $y = 0$, and $t = 2863$ s. Based on the Walén relation [*Landau and Lifshitz*, 1960], the perturbed shear component of plasma flow $\delta V_y = \pm A\delta V_{Ay}$ in shear Alfvén waves, with the Walén ratio $A = 1$ and the plus (minus) signs corresponding to $-\mathbf{k}_\parallel \parallel \mathbf{B}$ ($\mathbf{k}_\parallel \parallel \mathbf{B}$). The Walén relation has been found to be nearly satisfied at the magnetopause for ion flows and electron flows [*Sonnerup et al.*, 1981; *Scudder et al.*, 1999],

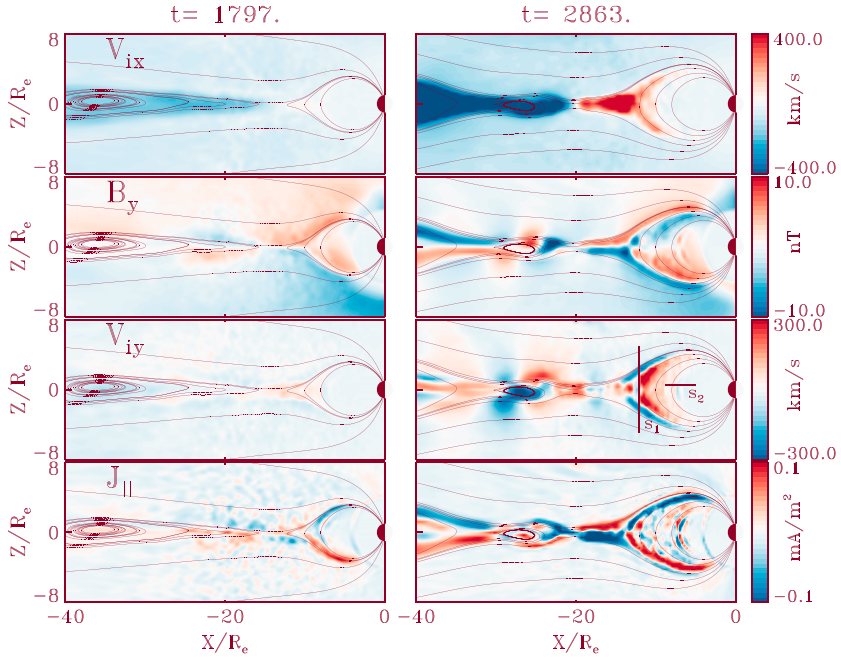

Figure 9. Contours of V_{ix}, B_y, V_{iy}, and $J_\parallel$ in the noon-midnight meridian plane at (left column) $t = 1797$ s and (right column) 2863 s show the propagation of Alfvén modes.

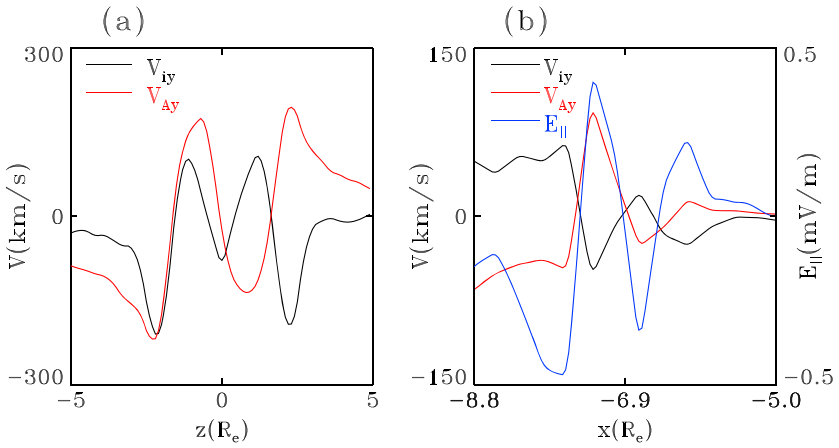

Figure 10. Structures of V_{iy} and V_{Ay} along (a) the line segment S_1 from $z = -5.0\ R_E$ to $+5.0\ R_E$ at $x = -12.0\ R_E$ and (b) the line segment S_2 from $x = -8.8\ R_E$ to $-5.0\ R_E$ at $z = +0.5\ R_E$, both for $t = 2863$ s and in the plane $y = 0$. Lines S_1 and S_2 are marked in the V_{iy} plot in Figure 9 (right column). The profile of the parallel electric field $E_\parallel$ is also plotted in Figure 10b to show the coherent structure in KAW.

with the ion Walén ratio ~ 0.7–0.9. The quantities V_{iy} and V_{Ay} in Figure 10a, which are approximately equal to the perturbed ones, are seen to be well correlated, with $V_{iy} \simeq -1.1V_{Ay}$ in $z > 0$ and $V_{iy} \simeq 0.7$–$1.0V_{Ay}$ in $z < 0$. Note that the temperature anisotropy is weak here and thus its modification to the Alfvén velocity can be ignored. The above result shows that the Walén relation is nearly satisfied in these waves. It demonstrates the propagation of Alfvén waves from the equator ($z \simeq 0$) to the north (along the direction of **B**) in the Northern Hemisphere and to the south (against **B**) in the Southern Hemisphere.

Earthward propagation of these waves from the tail leads to global Aflvénic structures in the geomagnetic dipole field. Alfvén waves propagate along field lines from the equator to the polar ionospheres, as shown in the global distribution of B_y, V_{iy}, and $J_\parallel$ in Figure 9 for $t = 2863$ s. An antiphase relation between perturbations in B_y and V_{iy} is seen clearly in the Northern Hemisphere, which demonstrates the propagation of Alfvén waves along the direction of **B**. In the Southern Hemisphere, the in-phase relation between B_y and V_{iy} corresponds to the propagation opposite to the **B** field.

Compared with the waves in the plasma sheet, the Alfvén waves in the dipole-like field region have evolved into shorter wavelength structures, as seen from $J_\parallel$, B_y, and V_{iy} around and earthward from the flow breaking at $x = -12\ R_E$. Figure 10b depicts V_{iy}, V_{Ay}, and the parallel electric field $E_\parallel$ along the line segment S_2 marked in the V_{iy} plot in Figure 9 (right column) from $x = -8.8\ R_E$ to $-5.0\ R_E$ at $z = +0.5\ R_E$, $y = 0$, and $t = 2863$ s. The ion flow component $V_{iy} \simeq -1.2$–$-0.8V_{Ay}$. The perpendicular wave number $k_\perp \rho_i \sim 1$ in these waves, together with the existence of a finite $E_\parallel$, consistent with being kinetic Alfvén waves [*Shi et al.*, 2013]. The parallel wavelength exhibits a global scale, with $k_\parallel << k_\perp$.

The formation of the KAWs globally in the dipole magnetosphere may be due to the radial inhomogeneity in the magnetic field, plasma density, and thus the Alfvén speed. The spatial variation of the wave propagation speed, V_A, in the continuous spectrum leads to the phase mixing of Alfvén waves [*Hong et al.*, 2012] from the tail and the generation of large $k_\perp$. Previous simulations have also shown that the interaction of the fast earthward flow and ion beams with the stationary near-Earth plasma can contribute to the generation of Alfvén waves [*Swift and Lin*, 2001; *Hong et al.*, 2008]. In addition, compressional waves from the plasma sheet and dipolarization front may be mode converted to KAWs and Alfvén waves as they propagate into the inhomogeneous plasma and magnetic field, due to the Alfvén resonance [*Hasegawa and Chen*, 1976; *Johnson and Cheng*, 1997; *Lin et al.*, 2012]. This way, the KAWs are generated globally, which is different from some other mechanisms in which the source of waves is local and thus the waves are damped with the propagation distance from the source. Associated with the Alfvénic perturbations are multiple field-aligned current filaments that are propagating to the auroral ionosphere, as seen in Figure 9 (bottom right).

4. Summary and Discussion

In this paper, a simulation is carried out for transport associated with the ion injection from the magnetotail to the inner magnetosphere, using a newly developed 3-D global hybrid simulation model. The simulation results of a case under a steady southward IMF are presented. The main results are summarized as follows.

1. Dayside reconnection leads to a plasma sheet thinning in the growth phase as the magnetic flux propagates into the magnetotail lobes, followed by magnetotail magnetic reconnection. The tail reconnection is triggered between $x = -15\ R_E$ and $-30\ R_E$ with multiple X lines, resulting in highly 3-D flux ropes.
2. A dawnward shift of plasma sheet plasmas is found during the thinning of the tail current sheet, mainly due to the particle $\mathbf{E}\times\mathbf{B}$ drift associated with the Hall electric field. The dawnward drift of ions is weakened after the tail reconnection takes place as more ions are unmagnetized. Such dawn-dusk asymmetry leads to the presence of more reconnection flux ropes on the duskside, where the density is lower than on the dawnside.
3. Bidirectional fast flows are generated from the tail reconnection. Because of the dawn-dusk asymmetry of the plasma sheet, more high-speed reconnection flows occur on the duskside than the dawnside. Due to the ion acceleration by reconnection, multiple ion beams are present in the plasma sheet, together with ion heating.
4. The ion acceleration causes significant ion injections from the tail to the inner magnetosphere. The flow injection first follows an earthward and dawnward/eastward direction and then diverges around the accumulated thermal pressure of the injected ions in the strong dipole-like field. The injected ions undergo the magnetic gradient and curvature drift in the dipole-like field, forming a ring current within $r = 5\ R_E$–$10\ R_E$. Outside the ring current, dawnward/eastward plasma flow is still observed on the dawnside.
5. The taillike field lines are dipolarized, and the dipole-like region expands following the impinging of magnetic flux and plasma on the inner magnetosphere. Fast-flow breaking is found at the dipolarization front. A reversal in the V_{ix} component of ion bulk flow motion is present on the dawnside of the ring current, and the dipolarization front undergoes a large-scale oscillation. The ion pressure builds up behind the front, where kinetic compressional turbulence with azimuthal wave propagation is visible in the magnetic field and plasma density. A sharp dip of magnetic field [*Runov et al.*, 2009] is present on the duskside of the dipolarization front, with a corresponding density peak. The cross-tail currents break into small-scale structures with $k_\perp \rho_i \sim 1$.
6. The dawn-dusk asymmetry also appears in the locally excited instabilities. Due to the countersteaming of the ring current ions from the tail and the tailward moving ions from the dayside LLBL, a shear flow-type instability is found on the duskside flank. Large $k_\perp$ structures are also present in the instability. On the other hand, a ballooning instability appears on the dawnside flank of the ring current, in the pressure buildup region, which leads to a radial plasma transport.
7. Alfvén waves and field-aligned currents, as well as compressional waves, are generated by reconnection and at the dipolarization front, which propagate to the ionosphere. KAWs with large $k_\perp \rho_i \sim 1$ are generated in the dipole-like field region, in which a significant radial variation exists in the Alfvén speed. Associated with the shear Alfvén waves/KAWs are multiple field-aligned current filaments above the auroral ionosphere.

The existence of the dawn-dusk asymmetry found in this simulation is caused by the ion particle drift effects, which do not exist in the MHD model. Although the case shown in this paper is only for a purely southward IMF, a similar dawn-dusk asymmetry of the plasma sheet due to the presence of the Hall electric field is expected to exist also for cases with a finite IMF B_y. Satellite observations and global MHD simulations have found that in the cases in which the IMF has a finite dawn-dusk component, a fraction of the IMF B_y can penetrate into the magnetotail [*Fairfield*, 1979; *Brecht et al.*, 1981; *Cao et al.*, 2014]. For a guide field smaller than or approximately the antiparallel field component, directions of the resulting E_x and E_z due to the Hall effects are expected to be similar to those in the cases with a zero guide field, but the detailed structures of the electric and magnetic field are altered[*Pritchett and Coroniti*, 2004]. The particle drift motion and the resulting structure of the tail current sheet are expected to be modified by the IMF B_y. The presence of more bursty bulk flows on the duskside is consistent with the scanned ion flow data from the THEMIS D spacecraft observation by *McPherron et al.* [2011], who found that earthward flows created by X lines are strongly localized in the local time sector 2100–0100. In a survey of the Geotail observations of magnetotail reconnection from 1996 to 2012, *Nagai et al.* [2013] have found that ion inflow-outflow structure shows a marked edge effect in the duskside plasma sheet. The inflow ions possess an additional dawnward motion.

Ballooning instability has been proposed as a possible candidate for substorm onset triggering. Several observations have reported the presence of the ballooning/interchange instability in the near tail around the midnight associated with the substorm onset[*Saito et al.*, 2008; *Panov et al.*, 2012]. But the presence, location, timing, and roles of the ballooning instability and its relation to BBFs and tail reconnection are still under debate. MHD simulations have found that the evolution of plasmoids can trigger ballooning instability[*Zhu et al.*, 2009], and ballooning instability can also induce plasmoids[*Zhu and Raeder*, 2014]. In the present global hybrid simulation, kinetic ballooning instability is present as a result of the pressure buildup due to the ion injection associated with the near-tail reconnection. Different from the above observations, in which the instabilities take place prior to the dipolarization onset, ballooning instabilities found in our simulation occur during the expansion. Moreover, the ballooning instabilities in our simulated case are present on the dawnside of the ring current, with ion $\beta \sim 3.4$, much smaller than that of *Saito et al.* [2008] for events in the plasma sheet. Based on the linear theory, similar growth rates of kinetic ballooning instability are predicted for conditions around midnight and the flank in the simulation. The reason for the lack of the ballooning instability at midnight may be that the region around midnight is dominated by the compressional wave turbulence due to the direct impact of BBF. It is noted that the larger convection speed used in the simulation has resulted in a faster development of turbulence. Further investigation and scaling studies are necessary to understand the triggering and global impacts of the kinetic ballooning instability.

The differences between our simulation and the observed events may be due to the very different IMF and solar wind conditions. On the other hand, in an observation of *Sakaguchi et al.* [2011] based on ground-based all-sky cameras, black aurora patches are linked to the interchange-type instability at the dipolarized flux tubes on the dawnside.

The presence of kinetic compressional waves and turbulence at the dipolarization front has been reported in satellite observations [*Huang et al.*, 2012; *Runov et al.*, 2012]. Propagation of kinetic Alfvén waves in the plasma sheet has also been reported by satellite observations [*Wygant et al.*, 2002; *Chaston et al.*, 2012]. Moreover, *Chaston et al.* [2014] have reported a Van Allen Probe observation of a kinetic-scale Alfvénic field line resonance during injections of energetic plasmas into the inner magnetosphere. In the plasma sheet, electromagnetic fluctuations of KAWs are embedded in the fast flow. It is believed that the energy of the injected plasmas from the magnetotail is coupled to resonating geomagnetic field lines on small scales. In our simulation, Alfvén waves and compressional waves are generated from the tail reconnection, and compressional waves are also excited due to the injected ions around the dipolarization front. The propagation of Alfvén waves and compressional waves to the inner magnetosphere leads to the generation of KAWs that propagate in the geomagnetic field, which provide a mechanism of energy deposit into the low-altitude magnetosphere and the ionosphere[*Chaston et al.*, 2014]. While it takes the response time of Alfvén waves for the energy buildup to large $k_\perp$ in the dipole-like field due to phase mixing, field line resonance and standing Alfvén waves may still be developed [*Lin and Wang*, 2005]. The evolution of Alfvén waves, field line resonance, and the impacts of KAWs to the aurora ionosphere demand further detailed investigations.

Three-dimensional global hybrid simulations, which resolve physics from the ion kinetic to global scales, are a powerful tool for investigation of the global dynamics of the magnetosphere. The present simulation is performed for a limited period of the global evolution that corresponds to ~40 min of the global convection time. A longer time simulation would be required to understand the nonlinear phases associated with the particle injection in a storm/substorm and their long-time global impacts.

Due to the computational constraint, the ion Larmor radius and the Alfvén speed used in the simulation are larger than those in reality. The geocentric distances of the magnetopause and plasma boundaries, on the other hand, are realistic because they are determined by the global quantities such as the IMF, geomagnetic field, and the solar wind Mach number. The scale sizes of wave and plasma structures in the simulated magnetosphere are larger than in the actual magnetosphere. Likewise, the local period in the simulation is larger than the global period by the same factor. This means that the evolution time of the local waves is effectively reduced, and thus, the growth and evolution of kinetic instabilities may be underestimated. A scaling study is necessary to understand the effects of the larger-particle scale on the nonlinear physics of kinetic instabilities. Previous MHD simulations have indicated that the Hall and Pederson conductances of the ionosphere have significant effects on the global dynamics *Raeder et al.* [2001]. The global hybrid simulation presented in this paper is for a case with a constant Pederson conductance. The dependence of the global structure, kinetic waves, and ion dynamics on the ionospheric boundary condition is not addressed.

Furthermore, the ring current in the hybrid simulation contains only the outer ring particles injected from the tail plasma sheet, which originated from the solar wind. The inner magnetosphere in the strong geomagnetic dipole-like field, with much faster time scales, is not accurately treated by this hybrid model. It is anticipated that the ring current dynamics will also impact the near-Earth magnetotail, but this is beyond the scope of this study.

Acknowledgments

This work was supported by NSF grant PHY-0903794 to Auburn University and grant 11235009 of the National Science Foundation of China. Computer resources were provided by the Alabama Supercomputer Center and Tianhe supercomputer center of China. Yu Lin thanks Simon Wing and Jay Johnson for helpful discussions. The authors also thank D.W. Swift for his help and discussions in the code development. The results in this paper are generated from our computer simulation code as described in section 2. The data can be obtained by contacting the authors through e-mail (ylin@physics.auburn.edu).

Michael Liemohn thanks Christopher Chaston and another reviewer for their assistance in evaluating the paper.

References

Angelopoulos, V., W. Baumjohann, C. F. Kennel, F. V. Coroniti, M. G. Kivelson, R. Pellat, R. J. Walker, H. Luhr, and G. Paschmann (1992), Bursty bulk flows in the inner central plasma sheet, *J. Geophys. Res.*, *97*, 4027–4039, doi:10.1029/91JA02701.

Angelopoulos, V., J. A. Chapman, F. S. Mozer, J. D. Scudder, C. T. Russell, K. Tsuruda, T. Mukai, T. J. Hughes, and K. Yumoto (2002), Plasma sheet electromagnetic power generation and its dissipation along auroral field lines, *J. Geophys. Res.*, *107*(A8), 1181, doi:10.1029/2001JA900136.

Angelopoulos, V., et al. (2008), Tail reconnection triggering substorm onset, *Science*, *321*, 931–935.

Angelopoulos, V., A. Runov, X.-Z. Zhou, D. L. Turner, S. A. Kiehas, S.-S. Li, and I. Shinohara (2013), Electromagnetic energy conversion at reconnection fronts, *Science*, *341*, 1478–1482, doi:10.1126/science.1236992.

Baker, D. N., T. I. Pulkkinen, V. Angelopoulos, W. Baumjohann, and R. L. McPherron (1996), Neutral line model of substorms: Past results and present view, *J. Geophys. Res.*, *101*, 12,975–13,010.

Baker, D. N., et al. (2006), A long-lived relativistic electron storage ring embedded in Earth's outer Van Allen belt, *Ann. Geophys.*, *24*, 1001–1013.

Bauer, T. M., W. Baumjohann, R. A. Treumann, and N. Sckopke (1995), Low-frequency waves in the near-Earth plasma sheet, *J. Geophys. Res.*, *100*, 9605–9617.

Birn, J., M. Hesse, and K. Schindler (1996), MHD simulations of magnetotail dynamics, *J. Geophys. Res.*, *101*, 12,939–12,954.

Birn, J., R. Nakamura, E. V. Panov, and M. Hesse (2011), Bursty bulk flows and dipolarization in MHD simulations of magnetotail reconnection, *J. Geophys. Res.*, *116*, A01210, doi:10.1029/2010JA016083.

Blake, J. B., W. A. Kolasinski, R. W. Fillius, and E. G. Mullen (1992), Injection of electrons and protons with energies of tens of Mev into L<3 on 24 March 1991, *Geophys. Res. Lett.*, *19*, 821–824.

Blanco-Cano, X., N. Omidi, and C. T. Russell (2009), Global hybrid simulations: Foreshock waves and cavitons under radial interplanetary magnetic field geometry, *J. Geophys. Res.*, *114*, A01216, doi:10.1029/2008JA013406.

Brecht, S. H., J. Lyon, J. A. Fedder, and K. Hain (1981), A simulation study of east-west IMF effects on the magnetosphere, *Geophys. Res. Lett.*, *8*, 397–400.

Buzulukova, N., M.-C. Fok, A. Pulkkinen, M. Kuznetsova, T. E. Moore, A. Glocer, P. Brandt, G. Toth, and L. Rastatter (2010), Dynamics of ring current and electric fields in the inner magnetosphere during disturbed periods: CRCM-BATS-R-US coupled model, *J. Geophys. Res.*, *115*, A05210, doi:10.1029/2009JA014621.

Cao, J. B., A. Duan, M. Dunlop, X. Wei, and C. Cai (2014), Dependence of IMF B_y penetration into the neutral sheet on IMF B_z and geomagnetic activity, *J. Geophys. Res. Space Physics*, *119*, 5279–5285, doi:10.1002/2014JA019827.

Chaston, C. C., J. R. Johnson, M. Wilber, M. Acuna, M. L. Goldstein, and H. Reme (2009), Kinetic Alfven wave turbulence and transport through a reconnection diffusion region, *Phys. Rev. Lett.*, *102*, 015001.

Chaston, C. C., J. W. Bonnell, L. Clausen, and V. Angelopoulos (2012), Correction to energy transport by kinetic-scale electromagnetic waves in fast plasma sheet flows, *J. Geophys. Res.*, *117*, A12205, doi:10.1029/2012JA018476.

Chaston, C. C., et al. (2014), Observations of kinetic scale field line resonances, *Geophys. Res. Lett.*, *41*, 209–215, doi:10.1002/2013GL058507.

Cheng, C. Z., and A. T. Y. Lui (1998), Kinetic ballooning instability for substorm onset and current disruption observed by AMPTE/CCE, *Geophys. Res. Lett.*, *25*, 4091–4094, doi:10.1029/1998GL900093.

Daglis, I. A., R. M. Thorne, W. Baumjohann, and S. Orsini (1999), The terrestrial ring current: Origin, formation, and decay, *Rev. Geophys.*, *37*, 407–438.

Dombeck, J., W. C. Cattell, J. R. Wygant, A. Keiling, and J. Scudder (2005), Alfven waves and Poynting flux observed simultaneously by Polar and FAST in the plasma sheet boundary layer, *J. Geophys. Res.*, *110*, A12S90, doi:10.1029/2005JA011269.

Drake, J. F. (1995), Magnetic reconnection: A kinetic treatment, in *Physics of the Magnetopause, Geophys. Monogr. Ser.*, vol. 90, edited by P. Song, B. U. Ö. Sonnerup, and M. F. Thomsen, p. 155, AGU, Washington, D. C.

Drake, J. F., M. Swisdak, T. D. Phan, P. A. Cassak, M. A. Shay, S. T. Lepri, R. P. Lin, E. Quataert, and T. H. Zurbuchen (2009), Ion heating resulting from pickup in magnetic reconnection exhausts, *J. Geophys. Res.*, *114*, A05111, doi:10.1029/2008JA013701.

El-Alaoui, M., R. L. Richard, M. Ashour-Abdalla, M. L. Goldstein, and R. J. Walker (2013), Dipolarization and turbulence in the plasma sheet during a substorm: THEMIS observations and global MHD simulations, *J. Geophys. Res. Space Physics*, *118*, 7752–7761, doi:10.1002/2013JA019322.

Eriksson, S., et al. (2004), Walén and slow-mode shock analyses in the near-Earth magnetotail in connection with a substorm onset on 27 August 2001, *J. Geophys. Res.*, *109*, A10212, doi:10.1029/2004JA010534.

Fairfield, D. H. (1979), On the average configuration of the geomagnetic tail, *J. Geophys. Res.*, *84*, 1950–1958.

Frey, H. U., S. B. Mende, V. Angelopoulos, and E. F. Donovan (2004), Substorm onset observations by IMAGE-FUV, *J. Geophys. Res.*, *109*, A10304, doi:10.1029/2004JA010607.

Ge, Y. S., J. Raeder, V. Angelopoulos, M. L. Gilson, and A. Runov (2011), Interaction of dipolarization fronts within multiple bursty bulk flows in global MHD simulations of a substorm on 27 February 2009, *J. Geophys. Res.*, *116*, A00I23, doi:10.1029/2010JA015758.

Ge, Y. S., X.-Z. Zhou, J. Liang, J. Raeder, M. L. Gilson, E. Donovan, V. Angelopoulos, and A. Runov (2012), Dipolarization fronts and associated auroral activities: 1. Conjugate observations and perspectives from global MHD simulations, *J. Geophys. Res.*, *117*, A10226, doi:10.1029/2012JA017676.

Hasegawa, A., and L. Chen (1976), Kinetic processes in plasma heating by resonant mode conversion of Alfven wave, *Phys. Fluids*, *19*, 1924–1934.

Hong, M. H., D. W. Swift, and Y. Lin (2008), Ion dynamics associated with Alfven waves in the near-Earth magnetotail: Two-dimensional global hybrid simulation, *Adv. Space Res.*, *41*, 1298–1304.

Hong, M. H., Y. Lin, and X. Y. Wang (2012), Generation of kinetic Alfvén waves by beam-plasma interaction in non-uniform plasma, *Phys. Plasmas*, *19*, 072,903, doi:10.1063/1.4736988.

Hu, Y. Q., X. C. Guo, and C. Wang (2007), On the ionospheric and reconnection potentials of the Earth: Results from global MHD simulations, *J. Geophys. Res.*, *112*, A07215, doi:10.1029/2006JA012145.

Huang, S. Y., M. Zhou, X. H. Deng, Z. G. Yuan, Y. Pang, Q. Wei, W. Su, H. M. Li, and Q. Q. Wang (2012), Kinetic structure and wave properties associated with sharp dipolarization front observed by Cluster, *Ann. Geophys.*, *30*, 97–107, doi:10.5194/angeo-30-97-2012.

Johnson, J. R., and C. Z. Cheng (1997), Kinetic Alfvén waves and plasma transport at the magnetopause, *Geophys. Res. Lett.*, *24*(11), 1423–1426, doi:10.1029/97GL01333.

Karimabadi, H., D. Krauss-Varban, N. Omidi, and H. X. Vu (1999), Magnetic structure of the reconnection layer and core field generation in plasmoids, *J. Geophys. Res.*, *104*, 12,313–12,326.

Karimabadi, H., H. X. Vu, D. Krauss-Varban, and Y. Omelchenko (2006), Global hybrid simulations of the Earth's magnetosphere, in *Numerical Modeling of Space Plasma Flows, ASP Conference Ser.*, vol. 359, edited by N. V. Pogorelov and G. P. Zank, p. 257, Astronomical Society of the Pacific, San Francisco, Calif.

Kivelson, M. G., and C. T. Russell (1995), *Introduction to Space Physics*, Cambridge Univ. Press, Cambridge, U. K.

Krauss-Varban, D., and N. Omidi (1995), Large-scale hybrid simulations of the magnetotail during reconnection, *Geophys. Res. Lett.*, *22*, 3271–3274.

Kuznetsova, M. M., M. Hesse, and D. Winske (1996), Ion dynamics in a hybrid simulation of magnetotail reconnection, *J. Geophys. Res.*, *101*, 27,351–27,373.

Landau, L. D., and E. M. Lifshitz (1960), *Electrodynamics of Continuous Media*, Pergamon, New York.

Lee, D.-Y., S. Ohtani, H. S. Kim, and K. C. Kim (2012), Observational test of interchange instability associated with magnetic dipolarization in the near-Earth plasma sheet of $r < 12R_E$, *J. Geophys. Res.*, *117*, A08206, doi:10.1029/2012JA017633.

Lin, Y., and D. W. Swift (1996), A two-dimensional hybrid simulation of the magnetotail reconnection layer, *J. Geophys. Res.*, *101*, 19,859–19,870.

Lin, Y., and D. W. Swift (2002), Generation of near-Earth reconnection by divergent flows in the plasma sheet, *J. Geophys. Res.*, *107*(A11), 1373, doi:10.1029/2002JA009308.

Lin, Y., and X. Y. Wang (2005), Three-dimensional global hybrid simulation of dayside dynamics associated with the quasi-parallel bow shock, *J. Geophys. Res.*, *110*, A12216, doi:10.1029/2005JA011243.

Lin, Y., J. R. Johnson, and X. Y. Wang (2012), Three-dimensional mode conversion associated with kinetic Alfven waves, *Phys. Rev. Lett.*, *109*, 125,003.

Liu, J., V. Angelopoulos, X.-Z. Zhou, and A. Runov (2014), Magnetic flux transport by dipolarizing flux bundles, *J. Geophys. Res. Space Physics*, *119*, 909–926, doi:10.1002/2013JA019395.

Lui, A. T. Y. (1996), Current disruption in the Earth's magnetosphere: Observations and models, *J. Geophys. Res.*, *101*, 13,067–13,088.

Lui, A. T. Y. (2009), Comment on "Tail reconnection triggering substorm onset", *Science*, *324*, 1391.

Lyon, J. G., R. E. Lopez, C. C. Goodrich, M. Wiltberger, and K. Papadopoulos (1998), Simulation of the March 9, 1995, substorm: Auroral brightening and the onset of lobe reconnection, *Geophys. Res. Lett.*, *25*, 3039–3042, doi:10.1029/98GL00662.

McPherron, R. L., T.-S. Hsu, J. Kissinger, X. Chu, and V. Angelopoulos (2011), Characteristics of plasma flows at the inner edge of the plasma sheet, *J. Geophys. Res.*, *116*, A00I33, doi:10.1029/2010JA015923.

Miura, A., S. Ohtani, and T. Tamao (1989), Ballooning instability and structure of diamagnetic hydromagnetic waves in a model magnetosphere, *J. Geophys. Res.*, *94*, 15,231–15,242.

Mobarry, C. M., J. A. Fedder, and J. G. Lyon (1996), Equatorial plasma convection from global simulations of the Earth's magnetosphere, *J. Geophys. Res.*, *101*, 7859–7874.

Nagai, T., M. Fujimoto, Y. Saito, S. Machida, T. Terasawa, R. Nakamura, T. Yamamoto, T. Mukai, A. Nishida, and S. Kokubun (1998), Structure and dynamics of magnetic reconnection for substorm onsets with Geotail observations, *J. Geophys. Res.*, *103*, 4419–4440.

Nagai, T., I. Shinohara, S. Zenitani, R. Nakamura, T. K. M. Nakamura, M. Fujimoto, Y. Saito, and T. Mukai (2013), Three-dimensional structure of magnetic reconnection in the magnetotail from Geotail observations, *J. Geophys. Res. Space Physics*, *118*, 1667–1678, doi:10.1002/jgra.50247.

Nishida, A., D. N. Baker, and S. W. H. Cowley (Eds.) (1998), *New Perspectives on the Earth's Magnetotail, Geophys. Monogr. Ser.*, vol. 105, AGU, Washington, D. C.

Nishimura, Y., L. Lyons, S. Zou, V. Angelopoulos, and S. B. Mende (2010), Substorm triggering by new plasma intrusion: THEMIS all-sky imager observations, *J. Geophys. Res.*, *115*, A07222, doi:10.1029/2009JA015166.

Ohtani, S., and J. Raeder (2004), Tail current surge: New insights from a global MHD simulation and comparison with satellite observations, *J. Geophys. Res.*, *109*, A01207, doi:10.1029/2002JA009750.

Omidi, N., X. Blanco-Cano, C. T. Russell, and H. Karimabadi (2006), Dipolar magnetospheres and their characterization as a function of magnetic moment, *Adv. Space Res.*, *33*, 1996–2003.

Panov, E. V., et al. (2010), Multiple overshoot and rebound of a bursty bulk flow, *Geophys. Res. Lett.*, *37*, L08103, doi:10.1029/2009GL041971.

Panov, E. V., V. A. Sergeev, P. L. Pritchett, F. V. Coroniti, R. Nakamura, W. Baumjohann, V. Angelopoulos, H. U. Auster, and J. P. McFadden (2012), Observations of kinetic ballooning/interchange instability signatures in the magnetotail, *Geophys. Res. Lett.*, *39*, L08110, doi:10.1029/2012GL051668.

Pontius D. H., Jr., and R. A. Wolf (1990), Transient flux tubes in the terrestrial magnetosphere, *Geophys. Res. Lett.*, *17*, 49–52.

Priest, E. R., and T. Forbes (2000), Definition of reconnection, in *Magnetic Reconnection: MHD Theory and Applications*, pp. 231–245, Cambridge Univ. Press, Cambridge, U. K.

Pritchett, P. L., and F. V. Coroniti (2004), Three-dimensional collisionless magnetic reconnection in the presence of a guide field, *J. Geophys. Res.*, *109*, A01220, doi:10.1029/2003JA009999.

Pritchett, P. L., and F. V. Coroniti (2010), A kinetic ballooning/interchange instability in the magnetotail, *J. Geophys. Res.*, *115*, A06301, doi:10.1029/2009JA014752.

Pulkkinen, T. I., D. N. Baker, M. Wiltberger, C. Goodrich, R. E. Lopez, and J. G. Lyon (1998), Pseudobreakup and substorm onset: Observations and MHD simulations compared, *J. Geophys. Res.*, *103*, 14,847–14,854, doi:10.1029/97JA03244.

Raeder, J., R. L. McPherron, L. A. Frank, S. Kokubun, G. Lu, T. Mukai, W. R. Paterson, J. B. Sigwarth, H. J. Singer, and J. A. Slavin (2001), Global simulation of the Geospace Environment Modeling substorm challenge event, *J. Geophys. Res.*, *106*, 381–395, doi:10.1029/2000JA000605.

Raeder, J., R. J. Walker, and M. Ashour-Abdalla (1995), The structure of the distant magnetotail during long periods of northward IMF, *Geophys. Res. Lett.*, *22*, 349–352.

Roux, A. (1985), Generation of field-aligned current structures at substorm onset, in *Proceedings of ESA Workshop on Future Missions in Solar, Heliospheric and Space Plasma Physics*, vol. SP-235, edited by E. Rolfe and B. Battrick, pp. 151–159, Eur. Space Agency Spec. Publ., Noordwijk, Netherlands.

Runov, A., V. Angelopoulos, M. I. Sitnov, V. A. Sergeev, J. Bonnell, J. P. McFadden, D. Larson, K.-H. Glassmeier, and U. Auster (2009), THEMIS observations of an earthward propagating dipolarization front, *Geophys. Res. Lett.*, *36*, L14106, doi:10.1029/2009GL038980.

Runov, A., V. Angelopoulos, and X.-Z. Zhou (2012), Multipoint observations of dipolarization front formation by magnetotail reconnection, *J. Geophys. Res.*, *117*, A05230, doi:10.1029/2011JA017361.

Saito, M. H., Y. Miyashita, M. Fujimoto, I. Shinohara, Y. Saito, K. Liou, and T. Mukai (2008), Ballooning mode waves prior to substorm-associated dipolarizations: Geotail observations, *Geophys. Res. Lett.*, *35*, L07103, doi:10.1029/2008GL033269.

Sakaguchi, K., K. Shiokawa, E. Donovan, A. Nakajima, Y. Hiraki, T. Trondsen, and F. Plaschke (2011), Periodic black auroral patches at the dawnside dipolarization front during a substorm, *J. Geophys. Res.*, *116*, A00I18, doi:10.1029/2010JA015957.

Scholer, M., and R.-F. Lottermoser (1998), On the kinetic structure of the magnetotail reconnection layer, *Geophys. Res. Lett.*, *25*, 3281–3284.

Scudder, J. D., P. Puhl-Quinn, F. S. Mozer, K. Ogilvie, and C. T. Russell (1999), Generalized Walén tests through Alfvén waves and rotational discontinuities using electron flow velocities, *J. Geophys. Res.*, *104*, 19,817–19,833.

Shay, M. A., J. F. Drake, J. P. Eastwood, and T. D. Phan (2011), Super-Alfvénic propagation of substorm reconnection signatures and Poynting flux, *Phys. Rev. Lett.*, *107*, 065,001.

Shi, F., Y. Lin, and X. Wang (2013), Global hybrid simulation of mode conversion at the dayside magnetopause, *J. Geophys. Res. Space Physics*, *118*, 6176–6187, doi:10.1002/jgra.50587.

Shue, J.-H., J. K. Chao, H. C. Fu, C. T. Russell, P. Song, K. K. Khurana, and H. J. Singer (1997), A new functional form to study the solar wind control of the magnetopause size, *J. Geophys. Res.*, *102*, 9497–9511.

Song, P., B. U. O. Sonnerup, and M. F. Thomson (Eds.) (1995), *Physics of the Magnetopause, Geophys. Monogr. Ser.*, vol. 90, AGU, Washington, D. C.

Sonnerup, B. U. O. (1979), Magnetic field reconnection, in *Solar System Plasma Physics*, vol. 3, edited by L. J. Lanzerotti, C. F. Kennel and E. N. Parker, pp. 46–108, North Holland, New York.

Sonnerup, B. U. O., G. Paschmann, I. Papamastorakis, N. Sckopke, G. Haerendel, S. J. Bame, J. R. Asbridge, J. T. Gosling, and C. T. Russell (1981), Evidence for magnetic reconnection at the Earth's magnetopause, *J. Geophys. Res.*, *86*, 10,049–10,067.

Swift, D. W. (1996), Use of a hybrid code for global-scale plasma simulation, *J. Comput. Phys.*, *126*, 109.

Swift, D. W., and Y. Lin (2001), Substorm simulation by use of a two-dimensional global-scale hybrid code, *J. Atmos. Sol. Terr. Phys.*, *63*, 683–704.

Takada, T., et al. (2006), Alfvén waves in the near-PSBL lobe: Cluster observations, *Ann. Geophys.*, *24*, 1001–1013.

Tan, B., Y. Lin, J. D. Perez, and X. Y. Wang (2011), Global-scale hybrid simulation of dayside magnetic reconnection under southward IMF: Structure and evolution of reconnection, *J. Geophys. Res.*, *116*, A02206, doi:10.1029/2010JA015580.

Tang, C. L., Z. Y. Li, V. Angelopoulos, S. B. Mende, K. H. Glassmeier, E. Donovan, C. T. Russell, and L. Lu (2009), THEMIS observations of the near-Earth plasma sheet during a substorm, *J. Geophys. Res.*, *114*, A09211, doi:10.1029/2008JA013729.

Terasawa, T. (1983), Hall current effects on tearing mode instabilities, *Geophys. Res. Lett.*, *10*, 475–478.

Vassiliadis, D., A. J. Klimas, S. G. Kanekal, D. N. Baker, and R. S. Weigel (2002), Long-term-average, solar cycle, and seasonal response of magnetospheric energetic electrons to the solar wind speed, *J. Geophys. Res.*, *107*(A11), 1383, doi:10.1029/2001JA000506.

Walker, R. J., T. Ogino, J. Reader, and M. Ashour-Abdalla (1993), A global magnetohydrohynamic simulation of the magnetosphere when the interplanetary magnetic field is southward: The onset of magnetotail reconnection, *J. Geophys. Res.*, *98*, 17,235–17,249.

Wing, S., and J. R. Johnson (2009), Substorm entropies, *J. Geophys. Res.*, *114*, A00D07, doi:10.1029/2008JA013989.

Wolf, R. A., Y. Wan, X. Xing, J.-C. Zhang, and S. Sazykin (2009), Entropy and plasma sheet transport, *J. Geophys. Res.*, *114*, A00D05, doi:10.1029/2009JA014044.

Wygant, J. R., et al. (2002), Evidence for kinetic Alfvén waves and parallel electron energization at 4-6 RE altitudes in the plasma sheet boundary layer, *J. Geophys. Res.*, *107*(A8), 1201, doi:10.1029/2001JA900113.

Yang, J., F. R. Toffoletto, R. A. Wolf, and S. Sazykin (2011), RCM-E simulation of ion acceleration during an idealized plasma sheet bubble injection, *J. Geophys. Res.*, *116*, A05207, doi:10.1029/2010JA016346.

Zhou, X.-Z., V. Angelopoulos, J. Liu, A. Runov, and S.-S. Li (2014), On the origin of pressure and magnetic perturbations ahead of dipolarization fronts, *J. Geophys. Res. Space Physics*, *119*, 211–220, doi:10.1002/2013JA019394.

Zhu, P., and J. Raeder (2014), Ballooning instability-induced plasmoid formation in near-Earth plasma sheet, *J. Geophys. Res. Space Physics*, *119*, 131–141, doi:10.1029/2013JA019511.

Zhu, P., J. Raeder, K. Germaschewski, and C. C. Hegna (2009), Initiation of ballooning instability in the near-Earth plasma sheet prior to the 23 March 2007 THEMIS substorm expansion onset, *Ann. Geophys.*, *27*, 1129–1138.

Zou, S., et al. (2010), Identification of substorm onset location and preonset sequence using Reimei, THEMIS GBO, PFISR, and Geotail, *J. Geophys. Res.*, *115*, A12309, doi:10.1029/2010JA015520.